

Structural basis for dimerization quality control

<https://doi.org/10.1038/s41586-020-2636-7>

Received: 21 October 2019

Accepted: 21 May 2020

Published online: 19 August 2020

 Check for updates

Elijah L. Mena^{1,6}, Predrag Jevtić^{1,2,7}, Basil J. Greber^{3,4,7}, Christine L. Gee^{1,2,7}, Brandon G. Lew^{1,2}, David Akopian¹, Eva Nogales^{1,2,3,4}, John Kuriyan^{1,2,3,4,5} & Michael Rape^{1,2,3}✉

Most quality control pathways target misfolded proteins to prevent toxic aggregation and neurodegeneration¹. Dimerization quality control further improves proteostasis by eliminating complexes of aberrant composition², but how it detects incorrect subunits remains unknown. Here we provide structural insight into target selection by SCF–FBXL17, a dimerization-quality-control E3 ligase that ubiquitylates and helps to degrade inactive heterodimers of BTB proteins while sparing functional homodimers. We find that SCF–FBXL17 disrupts aberrant BTB dimers that fail to stabilize an intermolecular β -sheet around a highly divergent β -strand of the BTB domain. Complex dissociation allows SCF–FBXL17 to wrap around a single BTB domain, resulting in robust ubiquitylation. SCF–FBXL17 therefore probes both shape and complementarity of BTB domains, a mechanism that is well suited to establish quality control of complex composition for recurrent interaction modules.

The signalling networks in metazoan development rely on recurrent interaction modules, such as BTB domains or zinc fingers, which often mediate specific dimerization events³. By forming stable homodimers^{4–7}, around 200 human BTB proteins control stress responses, cell division and differentiation^{8–17}. Extensive conservation of the BTB dimer interface causes frequent heterodimerization, which disrupts signalling and needs to be corrected for development to proceed².

Accordingly, dimerization quality control (DQC) by the E3 ligase SCF–FBXL17 degrades BTB dimers with wrong or mutant subunits, leaving active homodimers intact². BTB proteins could give rise to around 20,000 heterodimers and potentially more mutant complexes, but how SCF–FBXL17 can recognize such a wide variety of substrates while retaining specificity remains unknown. How SCF–FBXL17 discriminates complexes on the basis of composition is also unclear, especially as heterodimers contain the same subunits that are not recognized when forming homodimers. Here we addressed these issues by combining structural studies of substrate-bound SCF–FBXL17 with biochemical analyses of DQC target selection.

To generate SCF–FBXL17 substrates for structural investigation, we mutated residues near the dimerization helix of Kelch-like ECH-associated protein 1 (KEAP1), the BTB domain of which had been characterized by X-ray crystallography^{6,18}. As with other BTB proteins², FBXL17 detected KEAP1(F64A), KEAP1(V98A) and KEAP1(V99A), but not wild-type KEAP1, with submicromolar affinity (Fig. 1a, Extended Data Fig. 1a, b). Despite these differences in FBXL17 recognition, wild-type and mutant BTB domains formed dimers in size-exclusion chromatography (SEC) and SEC with multi-angle light scattering (SEC–MALS) analyses (Extended Data Fig. 1c, d). These dimers possessed similar stability towards unfolding by urea, with the unfolding of mutant BTB domains proceeding through an intermediate that might reflect local

conformational changes described below (Extended Data Fig. 1e, f). Crystal structures showed that KEAP1(F64A) and KEAP1(V98A) adopted the same BTB dimer fold as wild-type KEAP1 (Fig. 1b), with a C α root mean square deviation of approximately 0.2 Å between these proteins (Fig. 1b, Extended Data Fig. 1g). We conclude that FBXL17 must exploit features other than persistent structural changes to select substrates for DQC.

We therefore purified a SKP1–CUL1–F-box protein (SCF) complex comprising FBXL17, S-phase kinase-associated protein 1 (SKP1), the amino-terminal half of cullin 1 (CUL1) and KEAP1(V99A), and solved its cryo-electron microscopy (cryo-EM) structure to a resolution of 8.5 Å (Fig. 1c, Extended Data Figs. 2, 3a, b). We found that SCF–FBXL17 engaged the BTB domain of KEAP1(V99A) in a manner that is mutually exclusive with the interactions of KEAP1 with CUL3 (Fig. 1c, d). CUL3 did not prevent SCF–FBXL17 from ubiquitylating a BTB protein, suggesting that DQC is dominant over CUL3 (Extended Data Fig. 3c). The active site of SCF–FBXL17, marked by RBX1¹⁹, was next to the Kelch repeats of KEAP1(V99A) (Fig. 1c), and SCF–FBXL17 ubiquitylated BTB proteins with Kelch repeats more efficiently than BTB domains (Extended Data Fig. 3d, e). This suggests that substrate selection and ubiquitylation by SCF–FBXL17 occur in distinct target domains. Yet, the most notable feature of the structure was its stoichiometry: although KEAP1(V99A) formed dimers, SCF–FBXL17 bound a single BTB domain (Fig. 1c). This indicated that SCF–FBXL17 targets BTB dimers that dissociate more frequently or are split apart more easily than their homodimeric counterparts.

Focusing on the specificity determinant of DQC, we mixed SKP1–FBXL17 and the BTB domain of KEAP1(F64A) (Extended Data Fig. 4a) and obtained a 3.2 Å-resolution crystal structure of the resulting complex (Fig. 2a, Extended Data Table 1). The crystal structure fit well into the

¹Department of Molecular and Cell Biology, University of California at Berkeley, Berkeley, CA, USA. ²Howard Hughes Medical Institute, University of California at Berkeley, Berkeley, CA, USA.

³California Institute for Quantitative Biosciences (QB3), University of California at Berkeley, Berkeley, CA, USA. ⁴Molecular Biophysics and Integrative Bio-Imaging Division, Lawrence Berkeley National Laboratory, Berkeley, CA, USA. ⁵Department of Chemistry, University of California at Berkeley, Berkeley, CA, USA. ⁶Present address: Department of Genetics, Harvard Medical School, Boston, MA, USA. ⁷These authors contributed equally: Predrag Jevtić, Basil J. Greber, Christine L. Gee. ✉e-mail: mrape@berkeley.edu

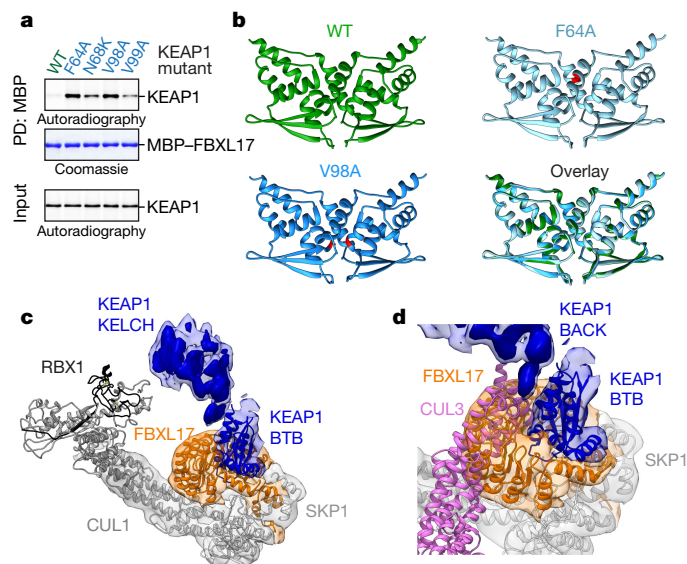


Fig. 1 | FBXL17 binds monomeric BTB domains. **a**, ³⁵S-labelled KEAP1 variants are recognized by immobilized FBXL17. Binding of mutant KEAP1 to FBXL17 was performed five times. PD, pull down; WT, wild type. **b**, Mutant (blue) and wild-type (green) KEAP1 BTB domains adopt the same dimer fold, as shown by X-ray crystallography at 2.2–2.5 Å resolution. **c**, The 8.5 Å-resolution cryo-EM structure of a complex between CUL1 (residues 1–410; medium grey); SKP1 (light grey); FBXL17 (orange); and KEAP1(V98A) (blue). X-ray coordinates of the FBXL17–SKP1–BTB complex (Fig. 2) and CUL1–RBX1²⁸ were fitted into the cryo-EM density. **d**, FBXL17 and CUL3 recognize overlapping surfaces on the BTB domain of KEAP1. CUL3 (magenta) was superposed onto the KEAP1 BTB domain based on Protein Data Bank (PDB) ID 5NLB.

map independently obtained by cryo-EM (Fig. 1c). As expected, FBXL17 uses its F-box to bind SKP1–CUL1 (Fig. 2a, Extended Data Fig. 4b, c), but is dependent on a domain of 12 leucine-rich repeats (LRRs) to recruit its targets. The LRRs of FBXL17 form a solenoid around the BTB domain, with residues in the last four LRRs directly engaging the substrate (Fig. 2b). The substrate-binding domain of FBXL17 is longer and more curved than that of other LRR proteins^{20,21} (Extended Data Fig. 4d), and closely follows the shape of the BTB domain (Fig. 2b). Downstream of its LRRs, FBXL17 contains a C-terminal helix (CTH), which enables FBXL17 to encircle the BTB domain (Fig. 2b–e). The CTH crosses the BTB dimer interface, which explains why FBXL17 ultimately binds single BTB domains (Fig. 2d, e). Structural models indicated that many BTB domains—which are similar in shape but distinct in sequence—could be accommodated by FBXL17 (Extended Data Fig. 4e); but the BTB-fold proteins SKP1 or elongin C—which are not substrates for DQC—would clash with FBXL17 (Extended Data Fig. 4f). In addition to confirming monomer capture, these results implicated the shape of BTB domains as a specificity determinant for DQC.

To validate our structures, we monitored the effects of FBXL17 mutations on target selection in cells. By investigating nascent KEAP1², we found that single mutations in FBXL17 rarely affected substrate binding or degradation (Fig. 3a–c, Extended Data Fig. 5a, b). By contrast, if mutations in LRRs and CTH were combined, recognition of KEAP1 by FBXL17 and its proteasomal degradation were obliterated (Fig. 3a–c). Our mutant collection showed that even residual binding to FBXL17 triggered degradation, as seen with the C574A/W626A or W626A/L677A variants of FBXL17. Proteomic analyses showed that combined LRR mutations or CTH deletion affected recognition of all BTB targets by FBXL17 (Fig. 3d). Whereas deletion of the CTH prevented recognition of BTB heterodimers (Fig. 3b–d, Extended Data Fig. 5c, d), the CTH by itself was unable to bind DQC targets (Extended Data Fig. 5c).

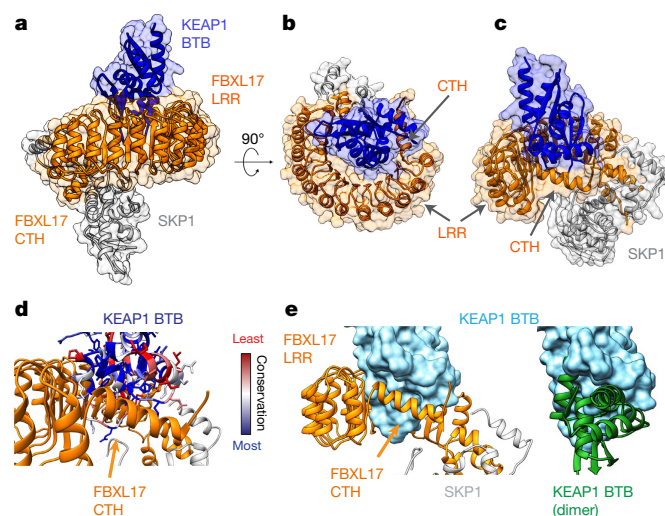


Fig. 2 | Crystal structure of substrate-bound FBXL17 reveals specificity determinants of DQC. **a**, Side view of the 3.2 Å X-ray structure of a complex between SKP1 (grey), FBXL17 (orange) and the BTB domain of KEAP1(F64A) (residues 48–180; blue). **b**, Top view of the SKP1–FBXL17–BTB complex showing how FBXL17 encircles the BTB domain with its LRRs and the CTH. **c**, Side view of the SKP1–FBXL17–BTB complex. **d**, The CTH binds a conserved area of the BTB domains (blue, high conservation; red, low conservation). **e**, The CTH crosses the dimerization interface of the BTB domain in a position typically occupied by another subunit in the BTB dimer (green).

Similarly, mutation of multiple KEAP1 residues at the interface with FBXL17 was required to abolish E3 binding and degradation (Fig. 3e, f, Extended Data Fig. 6a, b). Flexibility in substrate recognition was also implied by the observation that A60 of KLHL12², but not the corresponding A109 of KEAP1, was required for FBXL17 binding (Extended Data Fig. 6a), probably a consequence of KEAP1(A109) being slightly removed from the FBXL17 interface (Extended Data Fig. 6c). Combined with the relatively poor conservation of BTB residues at the interface with FBXL17 (Extended Data Fig. 7), these findings showed that FBXL17 can accommodate substantial sequence variation among BTB proteins to provide quality control against a large domain family.

We asked how DQC can discriminate between homodimers and heterodimers, even when they contain overlapping subunits. As FBXL17 ultimately captures BTB monomers, it might disrupt aberrant dimers, exploit spontaneous complex dissociation or a combination of these activities. Suggestive of complex disassembly, fluorescence resonance energy transfer (FRET) measurements showed that FBXL17, but not FBXL17(ΔCTH), caused dissociation of KEAP1(F64A) dimers (Fig. 4a, b, Extended Data Fig. 8a). Excess unlabelled KEAP1 or GroEL—which should capture monomers arising from spontaneous dimer disassembly—had only minor effects (Fig. 4a, b), and mixtures of BTB domains labelled with either FRET donor or acceptor did not establish substantial FRET after prolonged incubation (Extended Data Fig. 8b). Treatment of endogenous KLHL12 complexes with FBXL17, but not FBXL17(ΔCTH), also strongly reduced BTB heterodimerization (Extended Data Fig. 8c), and an FBXL17 variant that can bind but not ubiquitylate its targets inhibited KLHL12 heterodimerization in cells (Extended Data Fig. 8d).

Both modelling and sequential affinity purifications found that FBXL17 could initially engage BTB dimers (Extended Data Fig. 8e, f) if its CTH were displaced from the BTB interface (Extended Data Fig. 8f). Mutation of FBXL17 residues modelled close to the leaving BTB subunit also impaired substrate binding (Extended Data Fig. 8g), which suggested that a feature of BTB dimers allows FBXL17 select its targets. One such candidate feature was an intermolecular antiparallel β-sheet between a β-strand in the amino terminus of one subunit and a C-terminal β-strand of the interacting domain^{4,7}. In BTB monomers

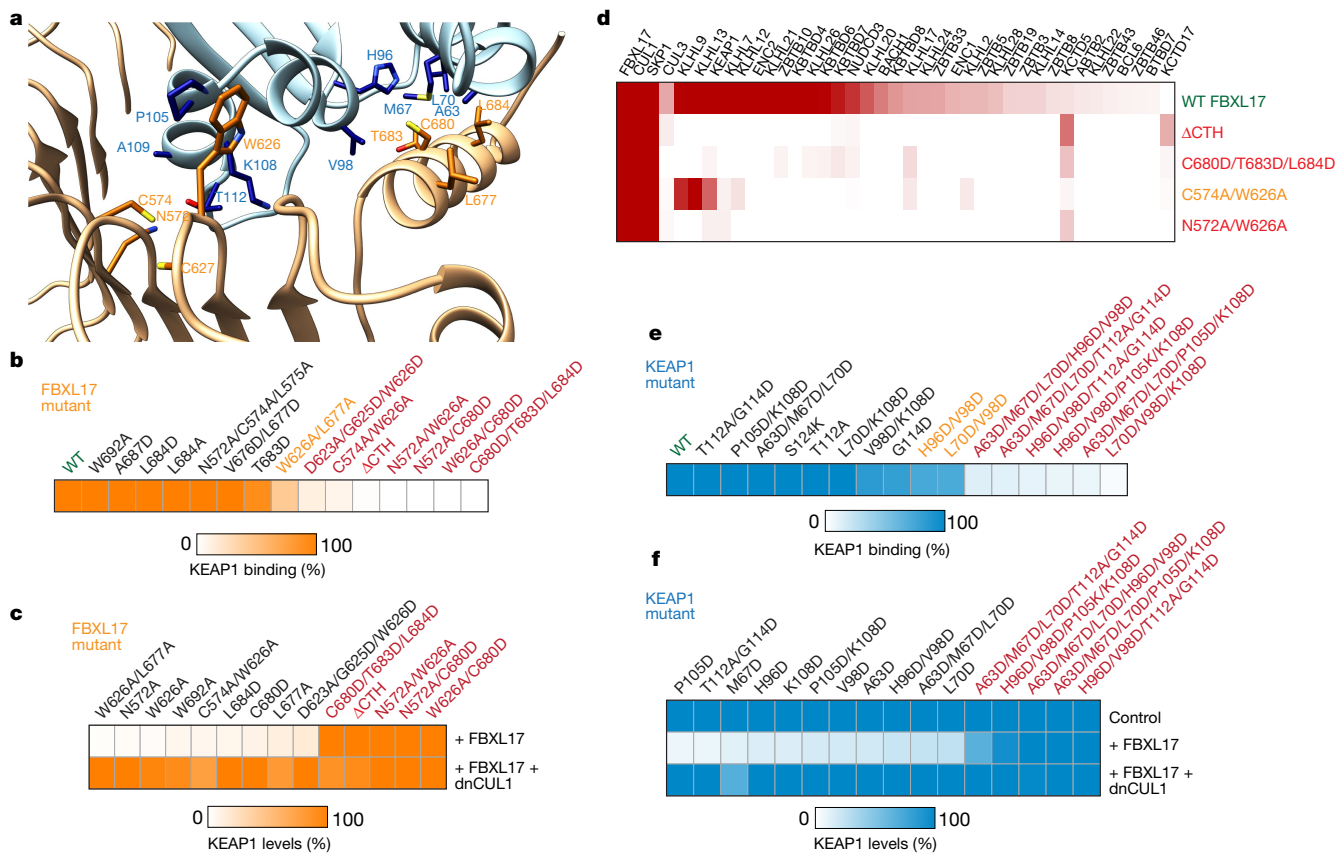


Fig. 3 | Multiple surfaces of FBXL17 contribute to substrate binding.

a, Detailed view of the interface between FBXL17 (orange) and the BTB domain of KEAP1 (F64A) (blue). **b**, Combined mutation of FBXL17 residues in LRRs and CTH prevents recognition of haemagglutinin (HA)-tagged KEAP1 (HA-KEAP1), as shown by FBXL17-Flag affinity purification and quantitative western blotting with HA antibody. **c**, Combined mutations in FBXL17 interfere with proteasomal degradation of KEAP1, as monitored by quantitative western

blotting. dnCUL1, dominant-negative CUL1. **d**, Mutations in FBXL17 prevent recognition of endogenous BTB proteins, as determined by affinity purification and mass spectrometry. The heat map shows total spectral counts normalized to FBXL17. **e**, Mutation of residues in HA-KEAP1 inhibits binding to FBXL17, as seen by FBXL17-Flag affinity purification and quantitative western blotting. **f**, Combined mutations in KEAP1 inhibit FBXL17-dependent degradation, as monitored by quantitative western blotting.

caught by FBXL17, the amino-terminal β -strand folds back onto its own C-terminal β -strand (Fig. 4c). As the intermolecular β -sheet must be dismantled for FBXL17 to capture BTB monomers, differences in its stability might allow substrate discrimination. Indeed, mutations that disrupt the domain-swapped β -sheet strongly promoted substrate recognition by FBXL17 (Fig. 4d), similar to deletion of the amino-terminal β -strand². FBXL17 binding was also stimulated by dimer-interface mutations, such as V50A in KLHL12 or F64A in KEAP1 (Fig. 1a, b, Extended Data Fig. 1a–d). Combining V50A in KLHL12 or F64A in KEAP1 with mutations in the β -strand did not further enhance substrate recognition by FBXL17 (Fig. 4d), suggesting that altering the dimer interface displaces the domain-swapped β -strand. Conversely, if we fused the amino terminus of KLHL12(V50A) to the C terminus of another BTB subunit to lock the β -strand in its dimer position, substrate recognition by FBXL17 was lost (Fig. 4e).

A structural model of KLHL12-KEAP1 heterodimers showed clashes only at the domain-swapped β -sheet and at neighbouring residues of the dimer interface (Fig. 4f). If we replaced clashing KLHL12 residues with those of KEAP1 to anchor the domain-swapped β -strand, the heterodimer escaped capture by FBXL17 (Fig. 4g). Conversely, if we introduced clashing KLHL12 residues into one subunit of KEAP1 homodimers to release the β -strand, the resulting complexes were readily detected by FBXL17 (Fig. 4h). When we transferred the same residues of KEAP1 into KLHL12, the chimeric KLHL12 formed heterodimers with KEAP1 in cells (Extended Data Fig. 9a), which were strongly impaired in their association with targets of either KLHL12 or KEAP1 (Extended Data

Fig. 9b, c). Thus, the domain-swapped β -sheet of BTB domains guides BTB dimerization and target selection by SCF-FBXL17. The β -sheet residues are highly divergent across BTB domains, with not a single β -strand being identical to another (Fig. 4i, Extended Data Fig. 10). This raises the possibility that the N-terminal β -strand evolved rapidly to constitute a molecular barcode for BTB dimerization that controls access to SCF-FBXL17.

On the basis of these findings, we propose that BTB homodimers form a robust domain-swapped β -sheet around their N-terminal β -strands to escape capture by SCF-FBXL17 (Fig. 5). By contrast, heterodimers or mutant dimers do not stabilize this β -sheet, which licenses them for detection and further destabilization by SCF-FBXL17. Dimer dissociation produces an unbound BTB subunit that can be immediately captured by other SCF-FBXL17 molecules. We expect that SCF-FBXL17 also binds BTB monomers that emerge upon spontaneous dissociation of heterodimers composed of distantly related BTB domains. SCF-FBXL17 finally wraps around and ubiquitylates single BTB domains that are similar in shape, but not necessarily in sequence. SCF-FBXL17 therefore selects its targets through a mechanism analogous to subunit exchange^{22–27}.

By probing complementarity and shape of BTB domains, SCF-FBXL17 discriminates complexes independently of the nature of specific subunits. Together with sequence variation accommodated by its large substrate-binding surface, this enables SCF-FBXL17 to target hundreds of heterodimers while ignoring the respective homodimers. This approach could be extended to other interaction modules, such

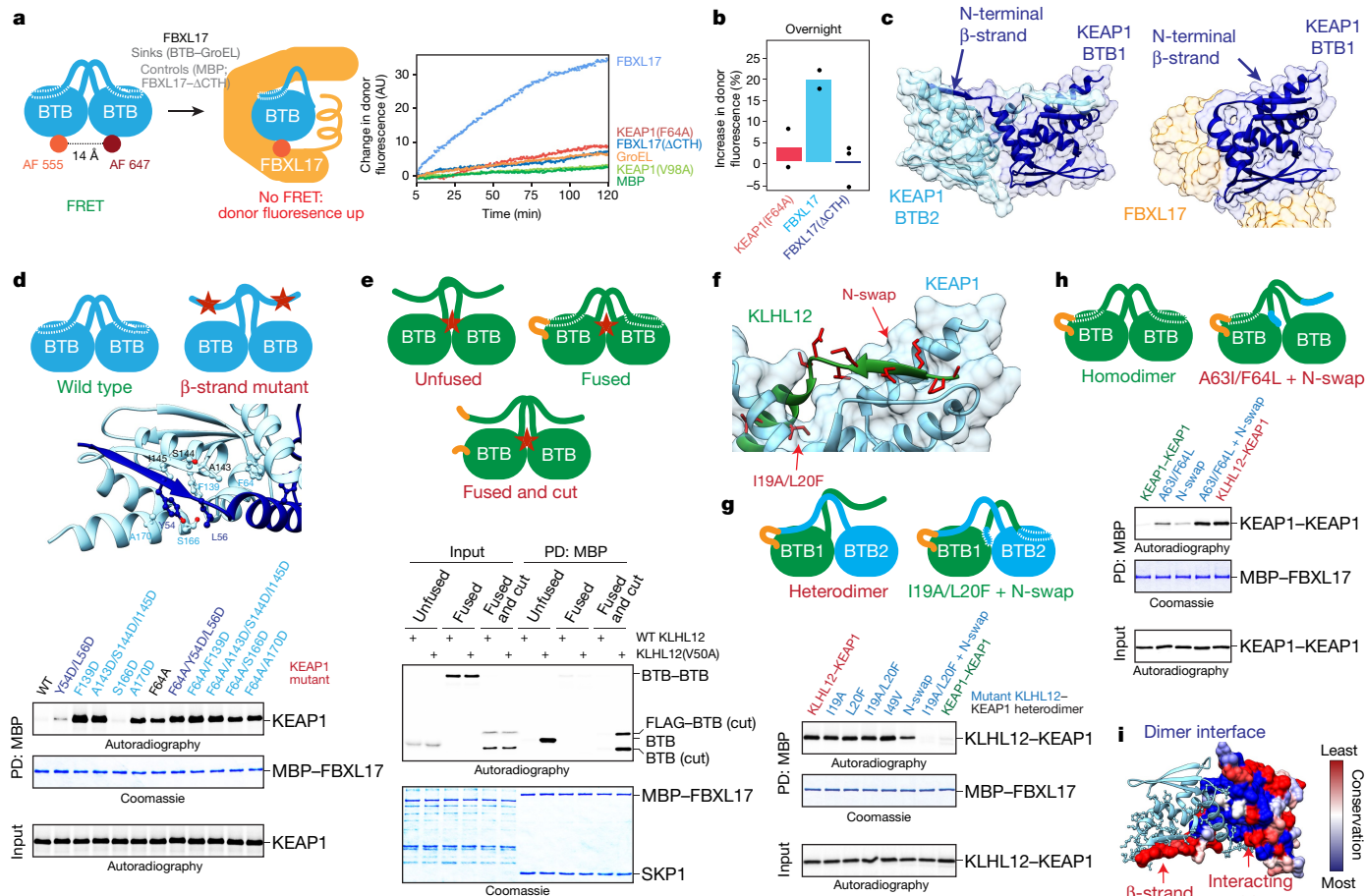


Fig. 4 | A domain-swapped β -sheet in BTB domains controls access to FBXL17. **a**, FRET assay. KEAP1(F64A) BTB dimers labelled with distinct fluorophores dissociate, as shown by loss of donor fluorescence quenching, upon incubation with FBXL17. Inactive FBXL17(Δ CTH), excess unlabelled BTB domains (KEAP1(F64A) and KEAP1(V98A)), GroEL or maltose-binding protein (MBP) did not have strong effects. Dissociation by FBXL17 was measured three times. AF 555, Alexa Fluor 555; AF 647, Alexa Fluor 647; AU, arbitrary units. **b**, Overnight incubation of FRET-labelled KEAP1(F64A) BTB dimers with FBXL17, FBXL17(Δ CTH) or excess unlabelled KEAP1(F64A) BTB domain. Dissociation was measured two or three times. **c**, The N-terminal β -strand of the KEAP1 BTB domain forms an intermolecular sheet in dimers, but adopts an intramolecular conformation in the BTB monomer bound to FBXL17. **d**, Binding of 35 S-labelled KEAP1 variants with mutations in the domain-swapped β -sheet to MBP-FBXL17. This experiment was performed once. **e**, 35 S-labelled unfused

BTB domains of KLHL12(V50A), fused BTB domains of KLHL12(V50A) or fused BTB domains that were cut within the linker were bound to MBP-FBXL17. Two independent experiments were performed with similar results. **f**, Structural model of a KLHL12-KEAP1 heterodimer shows clashes at the dimerization helix region and N-terminal β -strand. **g**, 35 S-labelled KLHL12-KEAP1 BTB heterodimers, mutant heterodimers and KEAP1 BTB homodimers were bound to MBP-FBXL17. Two independent experiments were performed with similar results. **h**, 35 S-labelled homodimeric KEAP1 (green), mutants with helix and β -strand residues of KLHL12 placed into the first subunit of a KEAP1 homodimer (blue), or KLHL12-KEAP1 heterodimers were incubated with MBP-FBXL17 and analysed for binding by gel electrophoresis and autoradiography. Two independent experiments were performed with similar results. **i**, The N-terminal β -strand and its interaction residues in the partner BTB domain evolve rapidly (blue, high conservation; red, no conservation).

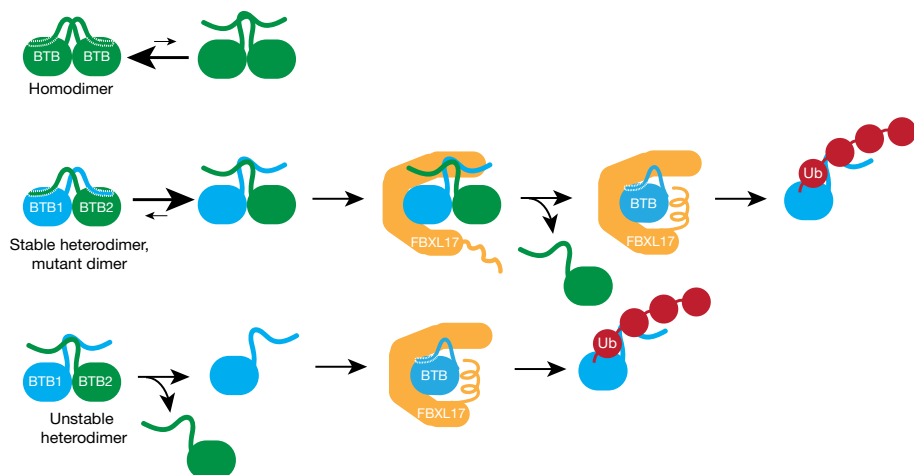


Fig. 5 | Model of the DQC mechanism. BTB homodimers have identical N-terminal β -strands mostly in the domain-swapped position. This prevents FBXL17 from engaging and ubiquitylating the homodimer. BTB heterodimers or mutant BTB dimers have poorly compatible helices and β -strands. Their N-terminal β -strands are mostly displaced, enabling capture of these aberrant dimers by FBXL17. FBXL17 may further destabilize these dimers or rely on spontaneous dimer dissociation to associate with a monomeric BTB subunit for ubiquitylation and degradation. Ub, ubiquitin.

as leucine zippers or zinc fingers, which mediate specific dimerization events. We anticipate that the mechanism described here will be of general importance for our understanding of quality control of complex composition.

Online content

Any methods, additional references, Nature Research reporting summaries, source data, extended data, supplementary information, acknowledgements, peer review information; details of author contributions and competing interests; and statements of data and code availability are available at <https://doi.org/10.1038/s41586-020-2636-7>.

- Balchin, D., Hayer-Hartl, M. & Hartl, F. U. In vivo aspects of protein folding and quality control. *Science* **353**, aac4354 (2016).
- Mena, E. L. et al. Dimerization quality control ensures neuronal development and survival. *Science* **362**, eaap8236 (2018).
- Gordley, R. M., Bugaj, L. J. & Lim, W. A. Modular engineering of cellular signaling proteins and networks. *Curr. Opin. Struct. Biol.* **39**, 106–114 (2016).
- Ji, A. X. & Privé, G. G. Crystal structure of KLHL3 in complex with Cullin3. *PLoS ONE* **8**, e60445 (2013).
- Zhuang, M. et al. Structures of SPOP-substrate complexes: insights into molecular architectures of BTB-Cul3 ubiquitin ligases. *Mol. Cell* **36**, 39–50 (2009).
- Cleasby, A. et al. Structure of the BTB domain of Keap1 and its interaction with the triterpenoid antagonist CDDO. *PLoS ONE* **9**, e98896 (2014).
- Ghetu, A. F. et al. Structure of a BCOR corepressor peptide in complex with the BCL6 BTB domain dimer. *Mol. Cell* **29**, 384–391 (2008).
- McGourty, C. A. et al. Regulation of the CUL3 ubiquitin ligase by a calcium-dependent co-adaptor. *Cell* **167**, 525–538 (2016).
- Werner, A. et al. Cell-fate determination by ubiquitin-dependent regulation of translation. *Nature* **525**, 523–527 (2015).
- Jin, L. et al. Ubiquitin-dependent regulation of COPII coat size and function. *Nature* **482**, 495–500 (2012).
- Furukawa, M. & Xiong, Y. BTB protein Keap1 targets antioxidant transcription factor Nrf2 for ubiquitination by the Cullin 3–Roc1 ligase. *Mol. Cell Biol.* **25**, 162–171 (2005).
- Wakabayashi, N. et al. Keap1-null mutation leads to postnatal lethality due to constitutive Nrf2 activation. *Nat. Genet.* **35**, 238–245 (2003).
- Louis-Dit-Picard, H. et al. *KLHL3* mutations cause familial hyperkalemic hypertension by impairing ion transport in the distal nephron. *Nat. Genet.* **44**, 456–460 (2012).
- Maerki, S. et al. The Cul3–KLHL21 E3 ubiquitin ligase targets aurora B to midzone microtubules in anaphase and is required for cytokinesis. *J. Cell Biol.* **187**, 791–800 (2009).
- Sumara, I. et al. A Cul3-based E3 ligase removes Aurora B from mitotic chromosomes, regulating mitotic progression and completion of cytokinesis in human cells. *Dev. Cell* **12**, 887–900 (2007).
- Duan, S. et al. FBXO11 targets BCL6 for degradation and is inactivated in diffuse large B-cell lymphomas. *Nature* **481**, 90–93 (2012).
- Tan, M. K., Lim, H. J., Bennett, E. J., Shi, Y. & Harper, J. W. Parallel SCF adaptor capture proteomics reveals a role for SCF^{FBXL17} in NRF2 activation via BACH1 repressor turnover. *Mol. Cell* **52**, 9–24 (2013).
- Yamamoto, M., Kensler, T. W. & Motohashi, H. The KEAP1–NRF2 system: a thiol-based sensor-effector apparatus for maintaining redox homeostasis. *Physiol. Rev.* **98**, 1169–1203 (2018).
- Zheng, N. et al. Structure of the Cul1–Rbx1–Skp1–F box^{Skp2} SCF ubiquitin ligase complex. *Nature* **416**, 703–709 (2002).
- Xing, W. et al. SCF^{FBXL3} ubiquitin ligase targets cryptochromes at their cofactor pocket. *Nature* **496**, 64–68 (2013).
- Schulman, B. A. et al. Insights into SCF ubiquitin ligases from the structure of the Skp1–Skp2 complex. *Nature* **408**, 381–386 (2000).
- Bhattacharyya, M. et al. Molecular mechanism of activation-triggered subunit exchange in Ca²⁺/calmodulin-dependent protein kinase II. *eLife* **5**, e13405 (2016).
- Pierce, N. W. et al. Cand1 promotes assembly of new SCF complexes through dynamic exchange of F box proteins. *Cell* **153**, 206–215 (2013).
- Reitsma, J. M. et al. Composition and regulation of the cellular repertoire of SCF ubiquitin ligases. *Cell* **171**, 1326–1339 (2017).
- Liu, X. et al. Cand1-mediated adaptive exchange mechanism enables variation in F-box protein expression. *Mol. Cell* **69**, 773–786 (2018).
- Wu, S. et al. CAND1 controls in vivo dynamics of the cullin 1–RING ubiquitin ligase repertoire. *Nat. Commun.* **4**, 1642 (2013).
- Zemla, A. et al. CSN- and CAND1-dependent remodelling of the budding yeast SCF complex. *Nat. Commun.* **4**, 1641 (2013).
- Duda, D. M. et al. Structural insights into NEDD8 activation of cullin–RING ligases: conformational control of conjugation. *Cell* **134**, 995–1006 (2008).

Publisher's note Springer Nature remains neutral with regard to jurisdictional claims in published maps and institutional affiliations.

© The Author(s), under exclusive licence to Springer Nature Limited 2020

Methods

Data reporting

No statistical methods were used to predetermine sample size. The experiments were not randomized. The investigators were not blinded to allocation during experiments and outcome assessment.

Plasmids and antibodies

All cDNAs for cellular and in vitro transcription and translation studies were cloned into pCS2+. For cellular experiments, FBXL17 was expressed as an active truncation, residues 310–701, with a C-terminal Flag tag². FBXL17(Δ CTH) encompassed residues 310–675 with a C-terminal Flag tag. FBXL17(Δ Fbox) encompassed residues 366–701 with a C-terminal Myc tag. KEAP1 point mutants were made in full-length constructs with an N-terminal 3 \times HA tag. KLHL12 and KEAP1 BTB fusions were based on constructs encompassing residues 6–129 of KLHL12 and residues 50–178 of KEAP1, separated by a GGGSGGG linker, and with a C-terminal HA tag. In the N-swap experiments, the N-terminal sequence was defined as residues 50–58 for KEAP1 and 6–14 for KLHL12 and was swapped for the N-terminal BTB in the respective fusion construct. Additional mutations in the N-terminal BTB of the fusions were made as annotated. The HRV 3C cleavable fusion constructs contained the same truncations but were instead separated by a GGGLEVLFGGGG linker sequence and they contained an N-terminal Flag tag instead of a C-terminal epitope tag. To generate chimeric KLHL12, a sequence encompassing residues 6–63 from the KLHL12 (N-swap + I19L/A20F) construct was amplified by PCR and ligated into full length KLHL12 construct with a C-terminal Flag in pCS2+. Additional constructs were generated: dominant negative (dn) Cull1 (residues 1–228 but without residues 59–82), 6 \times Myc–SKP1, KLHL12–3 \times Flag, KLHL12–HA and KEAP1–Flag. KLHL12(Δ CUL3) and KLHL12(Δ subs.) constructs were generated previously⁸. Point mutants were generated using Quikchange (Agilent).

Antibodies used in this study were: anti-Flag (CST, no. 2368, 1:5,000, lot 12), anti-HA (CST, no. 3724, clone C29F4, 1:15,000, lot 9), anti-Myc (Santa Cruz, no. sc-40, clone 9E10, lot B0519), anti-GAPDH (CST, no. 5174, clone D1GH11, 1:15,000, lot 7), anti- β -actin (MP Biomedicals, no. 691001, clone C4, 1:20,000, lot 04917), anti-SEC31A (BD, no. 612350, clone 32/Sec31A, 1:500, lot 8192947), anti-PEF1 (Abcam, no. ab137127, clone EPR9310, 1:500, lot GR104171-8), ALG2/PDCD6 (Proteintech, no. 12303-1-AP, clone AG2949, 1:500), anti-NRF2 (CST, no. 12721, clone D1Z9C, 1:1,000, lot 3), anti-KLHL12 (CST, no. 9406, clone 2G2, 1:1,000, lot 1), anti-KEAP1 (CST, no. 7705, clone D1G10, 1:1,000, lot 1), anti-KLHL9/13 (Santa Cruz, no. 166486, clone D-4, 1:1,000, lot F1011), anti-KBTBD6 (Abnova, no. H00089890-B01P, 1:500, lot G2191). The anti-KBTBD8 antibody was generated previously⁹ (1:250). For fluorescent western blot analysis we used secondary antibodies IRDye 800CW anti-rabbit (Li-Cor, no. 926-32211, 1:20,000, lot C90723-17). Blots were scanned on a Li-Cor Odyssey CLx instrument, and bands were quantified with ImageStudio. The normalized results were plotted as heat maps using Morpheus (<https://software.broadinstitute.org/morpheus>). Original uncropped western blots are presented in the Supplementary Information.

Cell culture analyses

We used HEK293T cells cultured in DMEM with GlutaMAX (Gibco, no. 10566-016) supplemented with 10% fetal bovine serum. HEK293T cells were purchased from the UC Berkeley Cell Culture Facility, authenticated by short tandem repeat analysis, and tested negative for mycoplasma contamination.

Transfections for immunoprecipitations were performed using polyethylenimine (PEI) (Polysciences, no. 23966-2) in a 1:6 ratio of μ g DNA: μ l PEI. The 6 \times Myc–SKP1 was also co-transfected with FBXL17 in a 3:1 ratio of FBXL17:SKP1. To perform the FBXL17 co-expression degradation assay 300,000 293T cells were seeded per well into 12-well plates 24 h before

transfection. We transfected 1 μ g DNA per well using 3 μ l Transit293 (Mirus, no. 2705). The ability of FBXL17 mutants to degrade the substrate was tested using the following four conditions: 50 ng wild-type (WT) KEAP1–HA, 950 ng pCS2+ vector; 50 ng WT KEAP1–HA, 300 ng WT FBXL17–Flag, 100 ng 6 \times Myc–SKP1, 550 ng pCS2+ vector; 50 ng WT KEAP1–HA, 300 ng mutant FBXL17–Flag, 100 ng 6 \times Myc–SKP1, 550 ng pCS2+ vector; 50 ng WT KEAP1–HA, 300 ng mutant FBXL17–Flag, 100 ng 6 \times Myc–SKP1, 550 ng pCS2+ vector, 150 ng dnCUL1. The degradation of KEAP1 mutants was tested using the following five conditions: 50 ng WT KEAP1–HA, 950 ng pCS2+ vector; 50 ng WT KEAP1–HA, 300 ng WT FBXL17–Flag, 100 ng 6 \times Myc–SKP1, 550 ng pCS2+ vector; 50 ng mutant KEAP1–HA, 950 ng pCS2+ vector; 50 ng mutant KEAP1–HA, 300 ng WT FBXL17–Flag, 100 ng 6 \times Myc–SKP1, 550 ng pCS2+ vector; 50 ng mutant KEAP1–HA, 300 ng WT FBXL17–Flag, 100 ng 6 \times Myc–SKP1, 550 ng pCS2+ vector, 150 ng dnCUL1. Cells were transfected for 36 h, washed, lysed using sample loading buffer and sonicated before western blot analysis.

Immunoprecipitations

Cells were transfected for 48 h, pelleted and resuspended in cold swelling buffer (20 mM HEPES–NaOH pH 7.5, 5 mM KCl, 1.5 mM MgCl₂) with 0.1% Triton-X100, 2 mM NaF, 0.2 mM Na₃VO₄ and protease inhibitors (Roche, no. 11873580001).

For transfections done in 10-cm plates, 500 μ l of swelling buffer was used to resuspend cells. For larger scales cells were resuspended in a 5:1 volume:mass ratio of buffer:pellet. Cells were lysed for 30 min on ice, freeze–thawed in liquid N₂ followed by 40 min centrifugation at 21,000g. Total protein concentration and volume of the lysate were normalized using Pierce 660 (Thermo, no. 22660). Normalized lysate was supplemented with NaCl to a final concentration of 150 mM and anti-Flag resin was added and incubated at 4 $^{\circ}$ C for 2 h. After four washes of the bound resin with cold wash buffer (20 mM HEPES–NaOH pH 7.5, 5 mM KCl, 1.5 mM MgCl₂, 0.1% Triton-X100, 150 mM NaCl) bound proteins were eluted by addition of sample loading buffer and analysed by western blotting.

For the KLHL12–FBXL17 sequential immunoprecipitation, KLHL12–3 \times Flag was purified with the anti-Flag resin and eluted with wash buffer supplemented with 0.5 mg ml^{−1} 3 \times Flag peptide (Sigma, no. F4799). The anti-HA resin (Sigma, EZview no. E6779) was blocked with 10% FBS for 20 min at 4 $^{\circ}$ C and washed once with wash buffer. The pre-blocked anti-HA resin was added to the elution supplemented with 10% FBS and incubated for 2 h at 4 $^{\circ}$ C. After three washes in wash buffer, sample loading buffer was added to the anti-HA resin, and samples were analysed by western blot.

For mass spectrometry, cells were transfected in 25 15-cm plates per condition (Fig. 3d, Extended Data Fig. 7d) or 40 plates per condition were used for endogenous KLHL12–3 \times Flag (Extended Data Fig. 7b, c). To prepare samples for mass spectrometry, bound proteins were eluted from anti-FLAG resin using 0.5 mg ml^{−1} 3 \times Flag peptide (Sigma, no. F4799), and proteins were precipitated overnight by the addition of trichloroacetic acid (Fisher, no. BP555) to a final concentration of 20% (w/v). Protein precipitates were washed three times in cold solution of 10 mM HCl in 90% acetone; resuspended in 8 M urea, 100 mM Tris–HCl, pH 8.5; reduced with 5 mM TCEP; and alkylated with 10 mM iodoacetamide. The samples were diluted with 100 mM Tris–HCl pH 8.5 to a 2 M urea concentration, supplemented with CaCl₂ to 1 mM concentration. Samples were trypsinized with 1 μ l of 0.5 mg ml^{−1} trypsin (Promega) overnight at 37 $^{\circ}$ C, and formic acid was added to 5% final concentration.

To test the effect of recombinant FBXL17 on endogenous KLHL12–3 \times Flag binding partners, anti-Flag resin bound with KLHL12 complexes were supplemented with 60 μ g of either His–MBP–FBXL17^{310–701}–SKP1, His–MBP–FBXL17(Δ CTH)^{310–675}–SKP1, or His–MBP and 500 μ l of PBST (PBS (Gibco, no. 14190144) + 0.1% Triton X-100) and rotated overnight at 4 $^{\circ}$ C. Resins were washed five times in cold wash buffer and further processed as described above.

Mass spectrometry

We used multidimensional protein identification technology (MudPIT) to analyse mass spectrometry samples. The analysis was performed by the Vincent J. Coates Proteomics/Mass Spectrometry Laboratory at UC Berkeley. To generate the interaction heat map, the normalized TSCs of select interactors in FBXL17 or BTB immunoprecipitates were plotted and higher values were set to 10 using default parameters of Morpheus (<https://software.broadinstitute.org/morpheus>).

Protein purifications

All KEAP1 BTB recombinant proteins were of the 48–180 truncation and contained the S172A mutation that enhanced crystallization⁶. KEAP1^{48–180}S172A, S172A/F64A, S172A/V98A, S172A/R116C and S172A/F64A/R116C mutants were cloned as a His–SUMO–TEV–KEAP1 fusion into the pET28a vector. They were transformed into *Escherichia coli* LOBSTR cells containing an RIL tRNA plasmid. Typically, 12 l of *E. coli* were grown to an OD₆₀₀ of 0.6, cooled to 16 °C, induced with 0.2 mM IPTG, and shaken at 16 °C overnight. Cell pellets were resuspended in lysis buffer (10% glycerol, 150 mM NaCl, 50 mM Tris-HCl pH 8.0, 5 mM β-mercaptoethanol, 10 mM imidazole pH 8.0, 1 mM PMSF and 1 mg ml⁻¹ lysozyme), lysed by sonication, and clarified by centrifugation at 38,000g for 30 min. Clarified lysate was incubated with Ni-NTA resin (Qiagen), washed with wash buffer (10% glycerol, 500 mM NaCl, 50 mM Tris/HCl pH 8.0, 10 mM imidazole pH 8.0, 5 mM β-mercaptoethanol), and eluted in a column with elution buffer (10% glycerol, 250 mM imidazole pH 8.0, 150 mM NaCl, 50 mM Tris-HCl pH 8.0, 5 mM β-mercaptoethanol). KEAP1 was dialysed overnight at 4 °C into buffer without imidazole (10% glycerol, 150 mM NaCl, 50 mM Tris-HCl pH 8.0, 5 mM β-mercaptoethanol), cut with TEV protease, and the tags were removed by Ni-NTA resin. KEAP1 was concentrated and then injected onto a HiLoad 16/600 Superdex 200 pg equilibrated with 150 mM NaCl, 25 mM Tris-HCl pH 8.0, and 1 mM TCEP at 4 °C. Fractions were pooled, concentrated to 11 mg ml⁻¹, and stored at –80 °C.

His–MBP–FBXL17^{310–701}–SKP1 and the ΔCTH variant (residues 310–675) were purified from insect cells as previously described². To purify SKP1–FBXL17^{310–701}–KEAP1^{BTB} complex for crystallography, we used a modified KEAP1^{BTB} construct that also contained a GST tag (His–SUMO*–GST–TEV–KEAP1(S172A/F64A)^{48–180}). KEAP1 protein was expressed and purified using Ni-NTA resin as described above and following the Ni elution it was bound to SKP1–His–MBP–FBXL17^{310–701} by mixing equal masses of SKP1–FBXL17 and KEAP1. After incubating the proteins overnight at 4 °C, KEAP1 was bound to glutathione Sepharose 2B resin (GE Healthcare), washed with 500 mM NaCl, 50 mM Tris-HCl pH 8.0, and 5 mM β-mercaptoethanol, and then eluted with 150 mM NaCl, 50 mM Tris-HCl pH 8.0, 5 mM β-mercaptoethanol, and 20 mM reduced glutathione (Sigma) by rotating at RT for 30 min. Following the glutathione elution, TEV was added for overnight cleavage at 4 °C. A subtractive Ni step was performed to remove the tags and then the protein complex was concentrated and injected at 4 °C onto a HiLoad 16/600 Superdex 200 pg equilibrated with 150 mM NaCl, 25 mM Tris-HCl pH 8.0, and 1 mM TCEP. Fractions were pooled, concentrated to 20 mg ml⁻¹, and stored at –80 °C.

CTH–MBP–His and MBP–His were subcloned into a pET28a vector with the CTH (residues 676–701 of FBXL17) and MBP separated by a GGS linker sequence. Constructs were expressed in *E. coli* LOBSTR cells and protein was purified using Ni-NTA resin, eluted with imidazole, and further purified using SEC.

The CUL1^{1–410}–SKP1–FBXL17^{310–701}–KEAP1(V99A) complex for cryo-EM was purified from High Five insect cells. Two pFastBac Dual constructs, one expressing FBXL17^{310–701} and SKP1 and another expressing KEAP1(V99A) (full-length) and CUL1^{1–410} were used to prepare separate baculoviruses according to standard protocols (Bac-to-Bac Baculovirus Expression System, Thermo Fisher). Several litres of High Five cells were split (1 × 10⁶ cells per ml) and infected with SKP1–FBXL17

and KEAP1–CUL1 baculoviruses (1% v/v for each) and grown at 27 °C for 3 days before collecting. Following collection, cells were resuspended in lysis buffer (50 mM Tris-HCl pH 8.5, 500 mM NaCl, 5 mM β-mercaptoethanol, 1 mM PMSF, 10 mM imidazole, 1% NP-40 substitute, 10% glycerol). After rotating at 4 °C for 30 min, lysate was clarified by centrifugation at 38,000g for 1 h. Supernatant was bound to Ni-NTA resin, washed with wash buffer (50 mM Tris-HCl pH 8.5, 500 mM NaCl, 5 mM β-mercaptoethanol, 10 mM imidazole pH 8.0, 10% glycerol) and eluted (50 mM Tris-HCl pH 8.5, 500 mM NaCl, 5 mM β-mercaptoethanol, 250 mM imidazole pH 8.0, 10% glycerol). The Ni elution was dialysed into buffer containing 50 mM Tris-HCl pH 8.5, 150 mM NaCl, and 5 mM β-mercaptoethanol and cut with TEV overnight at 4 °C. Protein was concentrated and injected onto a HiLoad 16/600 Superdex 200 pg equilibrated with 150 mM NaCl, 20 mM HEPES-NaOH pH 8.0, and 1 mM DTT. Fractions containing the quaternary complex were pooled, concentrated to 6 mg ml⁻¹, and stored at –80 °C.

The CUL1^{1–410}–SKP1–FBXL17^{310–701}–KEAP1^{V99A} cryo-EM complex was crosslinked using bis(sulfosuccinimidyl)suberate (BS3) (Thermo Fisher). The concentrated protein complex (24 μM) was supplemented with 1.4 mM BS3 cross-linker and incubated at room temperature for 30 min. The reaction was stopped by adding Tris-HCl pH 8.0 to 25 mM and incubating for an additional 10 min.

The recombinant CUL3^{1–197} for competition assays was cloned into pMAL-TEV–CUL3^{1–197}–His, expressed in BL21(DE3) cells and purified on amylose resin.

Crystallization and data collection

Crystals of KEAP1^{BTB} or the mutant variants were grown using the hanging vapour-diffusion method in 24-well plates. KEAP1 protein (11 mg ml⁻¹) was mixed in a 1:1 ratio with the reservoir solution. After 1–3 days at 20 °C, crystals with a needle morphology first appeared. By four days, crystals grew to dimensions of 25 μm × 25 μm × 800 μm. All of the KEAP1^{BTB}-only crystals used for structure determination were grown in wells containing reservoir solutions of 160–400 mM lithium acetate and 14–18% PEG 3350 (Hampton) as previously described⁶.

Crystals of the SKP1–FBXL17^{310–701}–KEAP1(F64A)–BTB complex were grown using the sitting-drop vapour-diffusion method by mixing 100 nl of 20 mg ml⁻¹ protein and 100 nl of reservoir solution within 96-well plates. After mixing, the plates were stored at 20 °C. Small rod-like crystals were first identified in the E7 condition (50 mM MgCl₂, 100 mM HEPES-NaOH pH 7.5, 30% (v/v) PEG MME 550) of the Index HT sparse matrix screen by Hampton. Crystals appeared after 1 day. Crystal growth was optimized by diluting the protein to 15 mg ml⁻¹ and by using a reservoir solution diluted to 75% (that is, 37.5 μl of E7 condition and 12.5 μl of water). By two days, crystals grew to 50 μm × 50 μm × 300 μm. Crystal growth was very sensitive to the volume of the drop (that is, no crystals formed in drops larger than 0.2 μl) and to the batch of E7 reservoir solution.

All crystals were cryo-protected by briefly soaking them in solutions containing the reservoir composition plus 20% (v/v) glycerol, before being plunged into liquid nitrogen. All data were collected on the Advanced Light Source beamline 8.3.1 at 100 K. Data collection and refinement statistics are presented in Extended Data Table 1.

X-ray crystal structure determination

Data were processed using XDS (version 26 January 2018)²⁹ and scaled and merged with Aimless (v.0.7.1)³⁰ in CCP4 (v.7.0.058)³¹. Structures were solved by molecular replacement using Phenix Phaser (v.2.8.2)³². The KEAP1 structures were solved by using the published KEAP1 dimer structure coordinates (PDB ID 4CXI). The SKP1–FBXL17–KEAP1^{BTB} complex structure was solved by searching for the KEAP1 core (residues 75–180 of PDB ID 4CXI), part of SKP1–SKP2 (all of SKP1 and the F-box of SKP2 (residues 95–137) in PDB ID 2ASS), and three LRRs of SKP2 (residues 204–279 in PDB ID 1FQV). Manual model building was performed in COOT (v.0.8.9.1)³³ and models were refined using Phenix refine (v.1.14)³².

Article

The initial SKP1–FBXL17–KEAP1^{BTB} complex model was improved using Phenix Rosetta Refine³⁴. The software used was curated by SBrGrid³⁵.

SEC analysis

All analytical size-exclusion runs were performed using an ÄKTA Pure (GE Healthcare) fitted with a Superdex 200 Increase 10/300 GL column or Superdex 75 Increase 10/300 GL column. The column was equilibrated with 150 mM NaCl, 50 mM Tris-HCl 8.0, 1 mM TCEP and runs were performed using a 0.2-ml injection loop and 0.5 ml min⁻¹ flow rate. Approximately 0.5 mg of protein was loaded. Molecular weight standards were purchased from Sigma-Aldrich.

SEC–MALS

Experiments were conducted using the Agilent Technologies 1100 series with a 1260 Infinity lamp, Dawn Heleos II and the Optilab T-Rex (Wyatt Technologies), and the Superdex 75 10/300 GL (GE Healthcare). The column was equilibrated with 50 mM Tris-HCl pH 8.0, 150 mM NaCl, and 1 mM TCEP at a rate of 0.5 ml min⁻¹ at room temperature. KEAP1 WT and F64A mutant were injected at a concentration of 2.5 mg ml⁻¹ in 100 μ l. A reference standard of bovine serum albumin was also injected at a concentration of 2 mg ml⁻¹ in 100 μ l. The refractive index was used to detect the mass in each peak and light scattering was used to detect the concentration and determine the molecular weight.

Denaturation monitored by circular dichroism

KEAP1 BTB domain proteins were exchanged into buffer containing 20 mM potassium phosphate pH 8.0, 50 mM NaCl, and 0.1 mM TCEP (CD buffer) using SEC. Both a 0 M and 8 M urea solution with 0.04 mg ml⁻¹ or 0.4 mg ml⁻¹ KEAP1 was made in CD buffer. These solutions were mixed in proportions to create a urea gradient series with 2.4 ml (low concentration) or 0.3 ml (high concentration) samples. These were equilibrated overnight at room temperature.

Circular dichroism recordings were taken using a 10-mm c cuvette (low concentration) or 1-mm cuvette (high concentration) on a AVIV model 410 CD spectrometer monitoring ellipticity at 222 nm. The signal was averaged over a 1-min interval, after a 1-min equilibration. Afterwards, each sample was measured using a Zeiss refractometer and the concentration of urea was calculated according to the fit³⁶: [Urea] = 11.766 \times Dh + 29.753 \times Dh² + 185.56 \times Dh³, in which Dh is the difference in refractive index between a given sample and the no denaturant sample.

The circular dichroism data points for wild-type KEAP1 were fit to a two-state unfolding curve:

$$Y_{\text{obs}} = \frac{(Y_u + S_u \times x) + (Y_f + S_f \times x)e^{-\frac{(\Delta G - m \times x)}{RT}}}{1 + e^{-\frac{(\Delta G - m \times x)}{RT}}},$$

in which x is urea concentration, Y_u is unfolded baseline y intercept, S_u is unfolded baseline slope, Y_f is folded baseline y intercept, S_f is folded baseline slope, m is the m -value (that is, the dependence of free energy of unfolding on urea concentration), and Y_{obs} is the recorded ellipticity values.

The circular dichroism data points for KEAP1 mutants were fit to a three-state unfolding curve³⁷:

$$Y_{\text{obs}} = \frac{(Y_u + S_u \times x) + (Y_i + S_i \times x)e^{-\frac{(G_1 - m_1 \times x)}{RT}} + (Y_f + S_f \times x)e^{-\frac{(G_2 - m_2 \times x)}{RT}}}{1 + e^{-\frac{(G_1 - m_1 \times x)}{RT}} + e^{-\frac{(G_2 - m_2 \times x)}{RT}} + e^{-\frac{(G_1 - m_1 \times x)}{RT}}},$$

in which additionally, Y_i is intermediate baseline y intercept, S_i is intermediate baseline slope, G_1 is ΔG between the folded and intermediate state, G_2 is ΔG between the intermediate and the unfolded state, m_1 is m -value between the folded and intermediate state and m_2 is m -value between the intermediate and unfolded state.

The equations were fitted to the data using the nls function in R and plotted in R. The C_m values were calculated from $C_m = \Delta G/m$.

In vitro assays

Full-length BTB proteins or isolated BTB domains in pCS2+ were synthesized using the TnT quick coupled rabbit reticulocyte lysate in vitro transcription and translation (IVTT) system (Promega, no. L2080). Each 12.5- μ l in vitro reaction contained 10 μ l of rabbit reticulocyte lysate, 0.2 μ l of ³⁵S-Methionine (11 μ Ci μ l⁻¹, Promega, no. NEG009H005MC), and 600 ng of pCS2+ construct. Reactions were mixed and incubated at 30 °C for 1 h. Approximately 10% of the IVTT was saved as input. The rest of reaction was mixed with 500 μ l PBST, 15 μ l amylose resin (NEB, no. E8021L), 8 μ g of His–MBP–FBXL17^{310–701}–SKP1 complex or His–MBP and incubated at 4 °C for 4 h. The resin was washed five times with cold PBST supplemented with 500 mM NaCl and eluted with the sample loading buffer. The pulldown was analysed by SDS–PAGE and autoradiography.

To test post-translational ubiquitylation of BTB proteins or isolated BTB domains, 12.5 μ l IVTT reactions were incubated for 45 min at 30 °C and stopped by addition of 0.5 μ l of 1.5 mg ml⁻¹ cycloheximide (Sigma, no. C7698; dissolved in 99% H₂O/1% DMSO). Reactions were supplemented with 1 μ l of 1 mg ml⁻¹ anti-Ub Tube1 (LifeSensors, UM101), 0.5 μ g of either His–MBP–FBXL17(WT)^{310–701}–SKP1 or His–MBP–FBXL17(Δ CTH)^{310–675}–SKP1. For CUL3 competition assay, 14 μ g of MBP–CUL3^{1–197} was added and incubated for 10 min at 30 °C before 0.5 μ g of His–MBP–FBXL17(WT)^{310–701}–SKP1 was added. Reactions were incubated for another 45 min at 30 °C, sample loading buffer was added, and ubiquitylation was analysed by SDS–PAGE and autoradiography.

In vitro titration reactions

Increasing concentrations of His–MBP–FBXL17(WT)^{310–701}–SKP1 were incubated with 60 μ l amylose resin (NEB, no. E8021L) at 4 °C for 4 h and washed three times in PBST. The bound resin was supplemented with 100 nM WT or F64A KEAP1^{48–180} in 400 μ l PBST and incubated for 1 h at room temperature. Reactions were centrifuged at 3,200 rpm for 1 min and the supernatant was removed and mixed with sample loading buffer. Samples were run on SDS–PAGE gels, stained with Coomassie, and imaged in a Li-COR Odyssey CLx. To analyse depletion of KEAP1^{48–180} from the supernatant, band intensities were quantified in ImageJ (v.1.51r), plotted in GraphPad Prism (v.8.3.0), and binding affinity was calculated using a nonlinear fit and binding-saturation equation.

Structural analysis and sequence alignments

The PISA server (<https://www.ebi.ac.uk/pdbe/pisa/>) was used to calculate the total surface interaction between FBXL17 and the KEAP1(F64A) BTB. PISA results were also used to determine which KEAP1 residues interacted with FBXL17, the opposing KEAP1 subunit, or CUL3 (PDB ID 5NLB) in their corresponding structures. Interacting residues were defined as containing at least 30% buried area.

The model of a KEAP1–KLHL12 heterodimer was determined by first obtaining a KLHL12 homodimer model from the SWISS-model server (<https://swissmodel.expasy.org>). One subunit of the KLHL12 homodimer was then aligned to one subunit within a KEAP1 wild-type homodimer. Clashing or incompatible regions were determined by manual inspection.

The map of conservation within the BTB domain was determined by first producing a sequence alignment using ClustalX (v.2.1) of 22 BTB substrates of FBXL17². Then the surface of KEAP1 was coloured by mavConservation according to a red–white–blue colour scheme.

Structural alignments of the KEAP1 BTB domains and the SKP1 and F-box structures were performed in Chimera (v.1.11). KLHL3 (PDB ID 4HXI), BCL6 (PDB ID 1R28), BACH1 (PDB ID 2IHC), SKP1 (PDB ID 1FS1), elongin C (PDB ID 4AJY), and the KLHL12 model generated from the SWISS-model server were aligned to the KEAP1 monomer in complex with FBXL17. The SKP1–FBXL3 (PDB ID 4I6J) and SKP1–SKP2 (PDB ID

2AST) structures were used for comparison with that of SKP1–FBXL17. Similarly, a KEAP1 homodimer was aligned to the SKP1–FBXL17–KEAP1 crystal structure in order to fit an opposing KEAP1 molecule (that is, the leaving BTB).

The sequence alignment of the N-terminal β -strand was created by first generating a sequence alignment of 55 dimeric-type BTB domains corresponding to KEAP1 residues 48–180 using ClustalX (v.2.1) with manual adjustment in Jalview (v.2.10.5). A neighbour-joining tree (of the full BTB domain) was calculated in Jalview using a BLOSUM62 scoring matrix. The N–J tree was then displayed using T-rex (<http://www.trex.uqam.ca>) and the sequence alignment of the β -strand region (KEAP1 residues 48–59) was coloured by residue in Jalview. A smaller number of BTB sequences was used in the full BTB alignment (Extended Data Fig. 7) and were displayed using ESPrnt 3 (<http://esprnt.ibcp.fr/ESPrnt/ESPrnt/>).

Cryo-EM specimen preparation and data collection

Graphene oxide coated cryo-EM grids were prepared based on Quantifoil UltraAuFoil R 1.2/1.3 (gold) grids. Carbon coated grids were prepared by floating a thin film of continuous carbon onto Quantifoil R 2/2 holey carbon grids. After drying overnight, the carbon-coated grids were glow discharged using a Cressington Sputter Coater (10 mA current, 13 s). Four μ l of crosslinked KEAP1–FBXL17–SKP1–CUL1 complex (approx. 2 μ M concentration) in buffer containing 150 mM NaCl, 20 mM HEPES–NaOH pH 7.5, 1 mM DTT, and 0.012% NP-40 substitute were applied to the carbon-coated, glow-discharged R2/2 grids, incubated for 1 min, blotted for 16–22 s in a Thermo Scientific VitroBot Mk IV, and flash-frozen by plunging into liquid ethane–propane cooled by liquid N₂ (ref. ³⁸). For graphene oxide-coated UltraAuFoil 1.2/1.3 grids, 4 μ l of KEAP1–FBXL17–SKP1–CUL1 complex at 2 μ M concentration were incubated for 30 s on the grid, blotted for 3.5–5 s, and flash-frozen.

Cryo-EM data were collected using a Thermo Scientific Talos Arctica transmission electron microscope operated at 200 kV acceleration voltage. Electron micrograph movies were collected in two sessions using Serial EM^{39,40}, one using particles on carbon support, one using particles on graphene oxide support. The dataset on carbon support was acquired using a Gatan K2 Summit direct electron detector camera, with the microscope set at 43,103 \times magnification, resulting in a pixel size of 1.16 Å, using a total dose of 50 electrons per Å² fractionated into 32 frames, and using a defocus range of –1.5 to –3.0 μ m; the dataset on graphene oxide was acquired using a Gatan K3 direct electron detector camera, at 43,860 \times magnification, resulting in a pixel size of 1.14 Å, using a total dose of 60 electrons per Å², fractionated into 53 frames, and by applying a defocus range of –2.0 to –3.0 μ m. We collected 545 micrographs of BS3-crosslinked KEAP1–FBXL17–SKP1–CUL1 complex (see above) on carbon support and 507 micrographs on graphene oxide support (example shown in Extended Data 2a).

Cryo-EM data processing

Electron micrograph movies were drift-corrected and dose-weighted using MOTIONCOR2⁴¹ from within FOCUS (v.1.1.10)⁴², or the motion correction algorithm implemented in RELION3⁴³. CTF parameters were estimated using GCTF⁴⁴ (carbon support dataset) and CTFIND⁴⁵ (graphene oxide dataset) from within RELION3, identifying 380 and 538 micrographs from the graphene oxide and carbon support datasets showing suitable quality than rings, respectively. All further data processing (Extended Data Fig. 2c, d) was performed in RELION3⁴³ unless stated otherwise.

Particles on graphene oxide. Particles were selected using the Laplacian-of-Gaussian algorithm implemented in RELION3⁴³. Picking was run separately for a subset of micrographs that showed gold edges in the images, which required different picking parameters owing to the high contrast of the gold areas. Overall, 542,436 particles were picked, extracted and rescaled to 3.42 Å per pixel. To remove images that

contain graphene oxide edges, the extracted particles were subjected to 2D classification. At this step, selecting the option to ignore the CTF until the first peak provided better results. Particles selected from gold edge-free and gold edge-containing micrographs were then joined, resulting in a dataset of 352,279 particle images. Based on previously obtained 3D references (see below), these particle images were classified into 6 3D classes, the best-resolved of which was selected for further processing. Adding further classes to the subsequent refinement did not improve the resolution in spite of the increased particle numbers, probably due to conformational differences between the classes. The 83,499 particles thus selected were first refined and then re-extracted with recentering, at 2.28 Å per pixel.

Particles on carbon support. Similarly to the graphene oxide dataset, 282,125 particles were picked using the Laplacian-of-Gaussian algorithm⁴³ and extracted at 2.32 Å per pixel. An initial 3D reference was obtained from this dataset by assembling a model from atomic coordinates according to the domain architecture inferred from 2D class averages (Extended Data Fig. 2d), which was then low-pass filtered to 40 Å resolution and iteratively subjected to 3D classification and refinement until a stable solution was obtained. Later ab initio 3D reconstruction in CRYOSPARC2⁴⁶ (Extended Data Fig. 2e) resulted in an initial model that was consistent with the previously described 3D reference and also allowed fitting of PDB coordinate models corresponding to CUL1, SKP1 and FBXL17–KEAP1, indicating retrieval of the correct solution (Extended Data Fig. 2e). Using the initial reference described above, the 282,125-particle dataset was classified into 4 3D classes; one class showing the best density features was selected and the resulting 76,757 particles were refined and re-extracted with recentering and rescaling to 2.28 Å per pixel.

The particles on carbon and graphene oxide support showed different orientation distributions (Extended Data Fig. 2c). Therefore, the particle subsets obtained from individual processing of the datasets of particles on graphene oxide and carbon support were joined to improve coverage of projection angles, thus reducing the risk of anisotropy in the reconstructed 3D map, and the resulting dataset of 160,256 particles was refined using two fully independent half-sets (gold standard⁴⁷). The resulting map was sharpened using a *B*-factor of –723 Å², determined automatically using the post-processing function in RELION, and low-pass filtered to 8.5 Å (Extended Data Fig. 2b) for visualization. Resolution is probably limited by the high flexibility of the KEAP1 KELCH domain and the tip of CUL1, which also show very low local resolution (Extended Data Fig. 2c).

Cryo-EM map interpretation

To interpret the cryo-EM map, we docked the atomic structures of the SKP1–FBXL17–KEAP^{BTB} complex (this work) as well as the structures of human SKP1 and CUL1 (PDB ID 1LDK)¹⁹ as rigid bodies using UCSF CHIMERA (v.1.13)⁴⁸. The N-terminal segment of the part of FBXL17 resolved in our structure (residues 319–362) was positioned independently to better fit the map due to a slight conformational difference between the X-ray crystal and cryo-EM structures. To resolve clashes at the interface between the rigid-body docked input models, we subsequently ran one macro cycle of PHENIX (v.1.16) real space refinement⁴⁹ using a map weight of 0.01 and restricting the information used to 10 Å. This procedure resolved the interface clashes as well as clashes and geometry outliers present in the CUL1 model used for docking (PDB ID 1LDK), while moving the C α atoms and non-clashing side chains only marginally (the C α R.M.S.D. for the FBXL17 portion of the structure before and after refinement is 0.2 Å).

Protein labelling for fluorescence energy transfer

We use maleimide chemistry to introduce FRET dyes on an introduced cysteine residue, R116C, which is not involved in dimerization or FBXL17 binding. To obtain homolabelled donor and acceptor variants

of KEAP1(F64A), KEAP1(S172A/F64A/R116C) was first exchanged into filtered, degassed DPBS using SEC and subsequently concentrated to 7 mg ml⁻¹. A 20 mM stock of Alexa Fluor 555 C2 maleimide (donor, Thermo Fisher, A20346) and Alexa Fluor 647 C2 maleimide (acceptor, Thermo Fisher, A20347) were independently created by dissolving 1 mg of solid dye in DMSO. KEAP1 was labelled in an overnight reaction in DPBS containing 100 μM protein, 20% degassed glycerol, and 1 mM of labelling dye. The reactions were quenched by adding β-mercaptoethanol to a final concentration of 10 mM, spun down at 21,000g for 10 min at 4 °C to eliminate any precipitation, and loaded onto a Superdex 200 Increase 10/300 GL equilibrated with 150 mM NaCl, 50 mM Tris-HCl 8.0, and 1 mM TCEP. Protein fractions containing dimeric KEAP1 were pooled and concentrated. Based on spectral comparisons of KEAP1(F64A/S172A) and KEAP1(F64A/S172A/R116C) labelling reactions, we estimate that >90% of the labelling was specific to the introduced cysteine and that >80% of molecules were labelled. The resulting homolabelled KEAP1(F64A) were then subjected to 8 M urea denaturation and refolding via dialysis overnight at room temperature, protected from light. The protein was then concentrated, spun at 21,000g for 10 min at 4 °C to eliminate any precipitation, and ran on a Superdex 200 Increase 10/300 GL column equilibrated with 150 mM NaCl, 50 mM Tris-HCl 8.0 and 1 mM TCEP. The fractions containing dimeric KEAP1 were collected and concentrated.

To obtain heterolabelled KEAP1(F64A), we mixed equimolar amounts of acceptor- and donor-labelled KEAP1(F64A/S172A/R116C), denatured by adding urea to 8 M, and refolded via dialysis overnight at room temperature in the dark. The protein was similarly concentrated, spun, and purified by SEC. The fractions containing dimeric KEAP1 were collected and concentrated.

Fluorescence resonance energy transfer assay and analysis

All FRET assays were conducted at 4 °C using a QuantaMaster QM4CW (PTI) fluorimeter and Hellma 105.251-QS cuvettes. Time courses followed the donor channel using an excitation of 555 nm and emission of 570 nm. Recordings were taken every 30 s for 2 h once 100 nM heterolabelled KEAP1 was mixed with 5 μM of chase protein. GroEL was obtained from Sigma-Aldrich (C7688). Overnight incubations were performed by taking spectra (555 nm excitation) of 100 nM heterolabelled KEAP1 dimer, followed by an overnight 4 °C incubation with 5 μM of chase protein. Similar measurements were performed for KEAP1 dimers labelled with either FRET donor or acceptor and then mixed. The bar graphs depicting percent increase in donor fluorescence upon addition of FBXL17, FBXL17(ΔCTH) or KEAP1(F64A) were calculated from emission at 570 nm. Calculations corrected for the dilution upon adding the chase protein.

Reporting summary

Further information on research design is available in the Nature Research Reporting Summary linked to this paper.

Data availability

The atomic coordinates of the CUL1-SKP1-FBXL17-KEAP1(V99A) complex has been deposited to PDB with accession number 6WCQ. The respective cryo-EM map has been deposited to the Electron Microscopy Data Bank with accession number EMD-21617. The atomic coordinates of the X-ray crystal structures have been deposited to the PDB with the following accession numbers: 6W66 (KEAP1(S172A/F64A)-FBXL17-SKP1 complex), 6W67 (KEAP1(S172A)), 6W68 (KEAP1(S172A/V98A)) and 6W69 (KEAP1(S172A/F64A)).

29. Kabsch, W. Xds. *Acta Crystallogr. D* **66**, 125–132 (2010).
30. Evans, P. R. & Murshudov, G. N. How good are my data and what is the resolution? *Acta Crystallogr. D* **69**, 1204–1214 (2013).
31. Winn, M. D. et al. Overview of the CCP4 suite and current developments. *Acta Crystallogr. D* **67**, 235–242 (2011).
32. Adams, P. D. et al. PHENIX: a comprehensive Python-based system for macromolecular structure solution. *Acta Crystallogr. D* **66**, 213–221 (2010).
33. Emsley, P., Lohkamp, B., Scott, W. G. & Cowtan, K. Features and development of Coot. *Acta Crystallogr. D* **66**, 486–501 (2010).
34. DiMaio, F. et al. Improved low-resolution crystallographic refinement with Phenix and Rosetta. *Nat. Methods* **10**, 1102–1104 (2013).
35. Morin, A. et al. Collaboration gets the most out of software. *eLife* **2**, e01456 (2013).
36. Grimsley, G. R., Huyghues-Despointes, B. M., Pace, C. N. & Scholtz, J. M. Preparation of urea and guanidinium chloride stock solutions for measuring denaturant-induced unfolding curves. *CSH Protoc.* **2006**, pdb.prot4241 (2006).
37. McDonald, S. K. & Fleming, K. G. Aromatic side chain water-to-lipid transfer free energies show a depth dependence across the membrane normal. *J. Am. Chem. Soc.* **138**, 7946–7950 (2016).
38. Tivol, W. F., Briegel, A. & Jensen, G. J. An improved cryogen for plunge freezing. *Microsc. Microanal.* **14**, 375–379 (2008).
39. Mastrorade, D. N. Automated electron microscope tomography using robust prediction of specimen movements. *J. Struct. Biol.* **152**, 36–51 (2005).
40. Schorb, M., Haberbosch, I., Hagen, W. J. H., Schwab, Y. & Mastrorade, D. N. Software tools for automated transmission electron microscopy. *Nat. Methods* **16**, 471–477 (2019).
41. Zheng, S. Q. et al. MotionCorr2: anisotropic correction of beam-induced motion for improved cryo-electron microscopy. *Nat. Methods* **14**, 331–332 (2017).
42. Biyani, N. et al. Focus: The interface between data collection and data processing in cryo-EM. *J. Struct. Biol.* **198**, 124–133 (2017).
43. Zivanov, J. et al. New tools for automated high-resolution cryo-EM structure determination in RELION-3. *eLife* **7**, e42166 (2018).
44. Zhang, K. Gctf: Real-time CTF determination and correction. *J. Struct. Biol.* **193**, 1–12 (2016).
45. Rohou, A. & Grigorieff, N. CTFFIND4: Fast and accurate defocus estimation from electron micrographs. *J. Struct. Biol.* **192**, 216–221 (2015).
46. Punjani, A., Rubinstein, J. L., Fleet, D. J. & Brubaker, M. A. cryoSPARC: algorithms for rapid unsupervised cryo-EM structure determination. *Nat. Methods* **14**, 290–296 (2017).
47. Scheres, S. H. W. & Chen, S. Prevention of overfitting in cryo-EM structure determination. *Nat. Methods* **9**, 853–854 (2012).
48. Pettersen, E. F. et al. UCSF Chimera—a visualization system for exploratory research and analysis. *J. Comput. Chem.* **25**, 1605–1612 (2004).
49. Afonine, P. V. et al. Real-space refinement in PHENIX for cryo-EM and crystallography. *Acta Crystallogr. D* **74**, 531–544 (2018).
50. Rosenthal, P. B. & Henderson, R. Optimal determination of particle orientation, absolute hand, and contrast loss in single-particle electron cryomicroscopy. *J. Mol. Biol.* **333**, 721–745 (2003).

Acknowledgements We thank C. Nixon, S. Costello and S. Marqusee for their generous help with circular dichroism; members of the A. Martin laboratory for their help with FRET; L. Nocka for help with SEC-MALS; F. Rodriguez Perez for help with R; A. Patel and D. Toso for help with graphene oxide grid preparation and cryo-EM data collection, respectively; J. Holton and G. Meigs at the Advanced Light Source Beamline 8.3.1 for assistance with data collection; J. Schaletzky for her comments on the manuscript; and members of the Rape, Nogales and Kuriyan laboratories for discussion and suggestions. Beamline 8.3.1 at the Advanced Light Source is operated by the University of California Office of the President, Multicampus Research Programs and Initiatives grant MR-15-328599, the National Institutes of Health (R01 GM124149 and P30 GM124169), Plexikon and the Integrated Diffraction Analysis Technologies program of the US Department of Energy Office of Biological and Environmental Research. The Advanced Light Source (Berkeley) is a national user facility operated by Lawrence Berkeley National Laboratory on behalf of the US Department of Energy under contract number DE-AC02-05CH11231, Office of Basic Energy Sciences. E.L.M. was funded by an NSF predoctoral scholarship (ID 2013157149). B.J.G. was supported by fellowships from the Swiss National Science Foundation (projects P300PA_160983, P300PA_174355). P.J. was funded by a Siebel Institute postdoctoral fellowship. D.A. was funded by an NIH F32 postdoctoral fellowship. E.N., J.K. and M.R. are investigators with the Howard Hughes Medical Institute.

Author contributions E.L.M., B.G.L. and D.A. purified recombinant proteins and performed SEC, SEC-MALS, CD and FRET experiments. E.L.M., B.G.L. and C.L.G. performed crystallization experiments. B.J.G. and E.L.M. performed cryo-EM experiments. P.J. performed immunoprecipitation, degradation and mass spectrometry analyses. E.L.M. and P.J. performed in vitro binding assays. P.J. and E.L.M. performed in vitro ubiquitylation assays. P.J. and D.A. performed in vitro titration assays. All authors interpreted the data and wrote the manuscript.

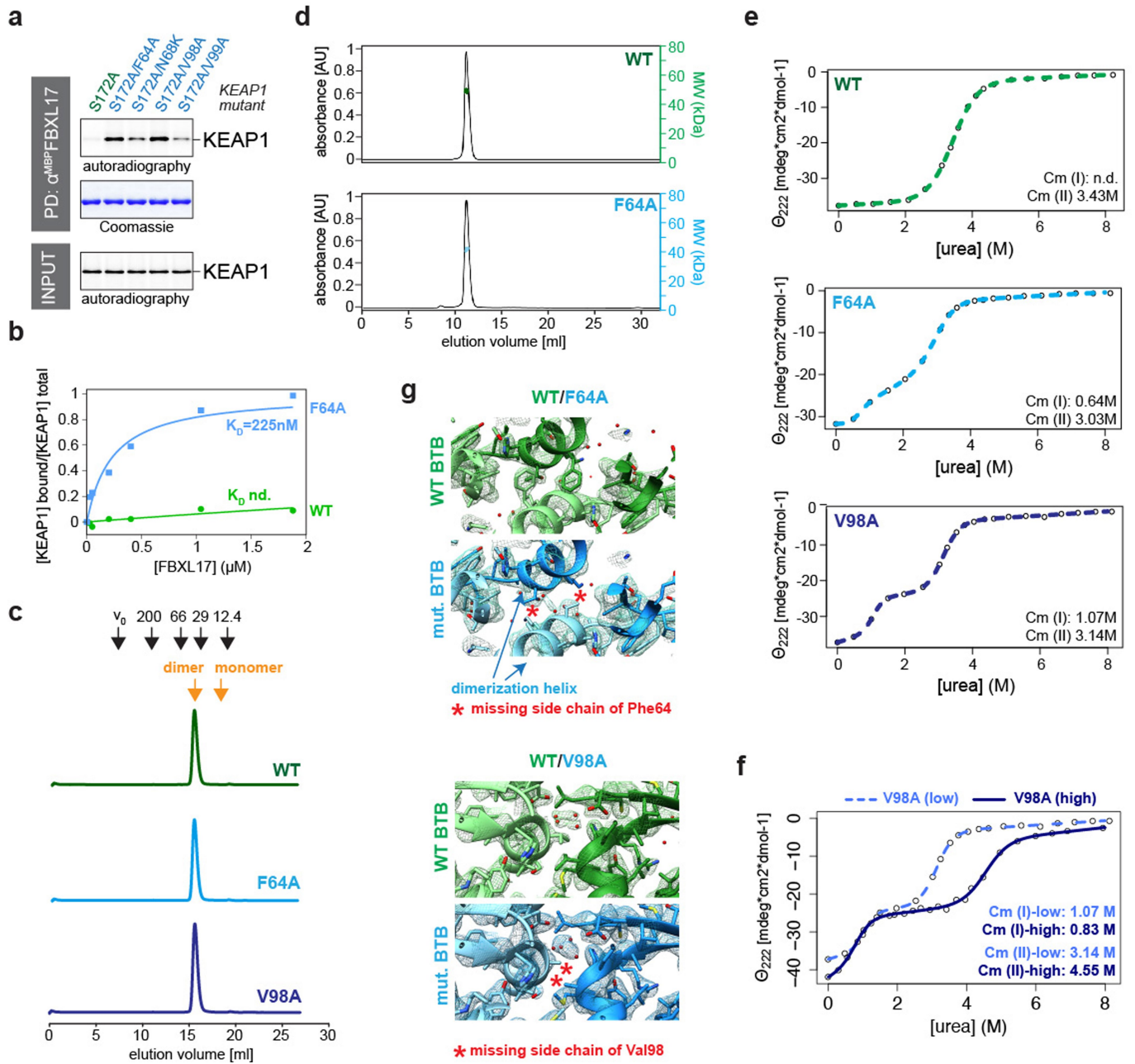
Competing interests M.R. and J.K. are founders and consultants of Nurix, a biotechnology company working in the ubiquitin field.

Additional information

Supplementary information is available for this paper at <https://doi.org/10.1038/s41586-020-2636-7>.

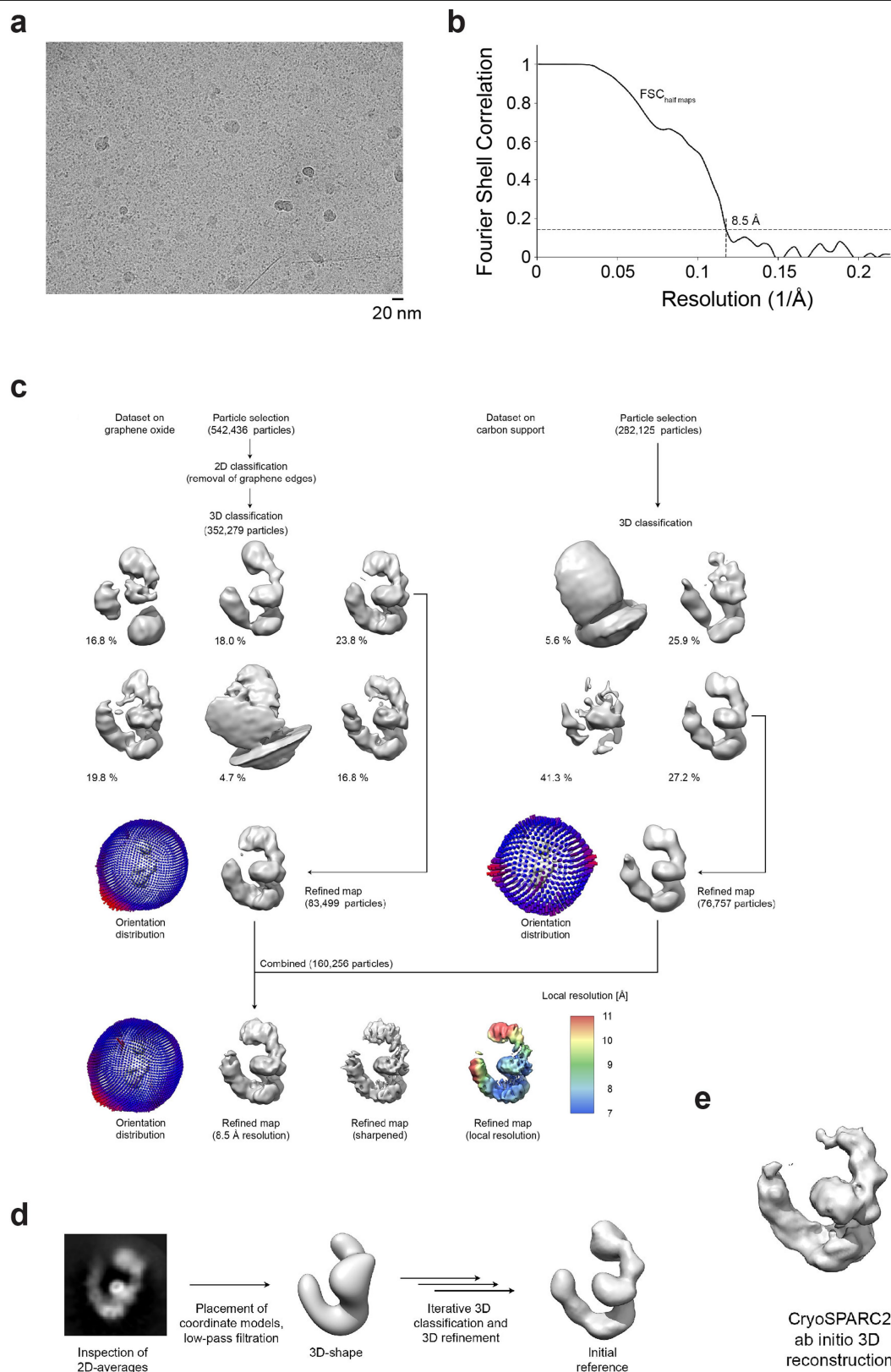
Correspondence and requests for materials should be addressed to M.R.

Reprints and permissions information is available at <http://www.nature.com/reprints>.



Extended Data Fig. 1 | Variant BTB domains of KEAP1 are recognized by SCF^{FBXL17}. **a**, Mutations in KEAP1's BTB domain result in efficient recognition by SCF^{FBXL17}. The same mutations as in Fig. 1a were introduced into the KEAP1^{S172A} variant that had previously been used for crystallization. ³⁵S-labelled double mutants, but not the KEAP1^{S172A} single mutant, were retained by immobilized MBP^{FBXL17}, as detected by gel electrophoresis and autoradiography. This experiment was performed once. **b**, SCF^{FBXL17} strongly prefers mutant over wild-type BTB domains. Increasing concentrations of MBP^{FBXL17} were immobilized on amylose beads and incubated with 100 nM wild-type or mutant KEAP1. Depletion of KEAP1 from the supernatant was measured by quantitative LiCor imaging of Coomassie-stained SDS-PAGE gels. The affinity of FBXL17 to wild-type KEAP1 was too low to be determined reliably by this method. Three independent experiments were performed with similar results. **c**, Mutant BTB domains form homodimers in vitro. Recombinant BTB domains of KEAP1, KEAP1^{F64A}, and KEAP1^{V98A} (MW about 15 kDa) were analysed by size exclusion chromatography detecting A₂₈₀. Expected position of BTB dimer versus monomer, as well as of control proteins with known MW are shown on top.

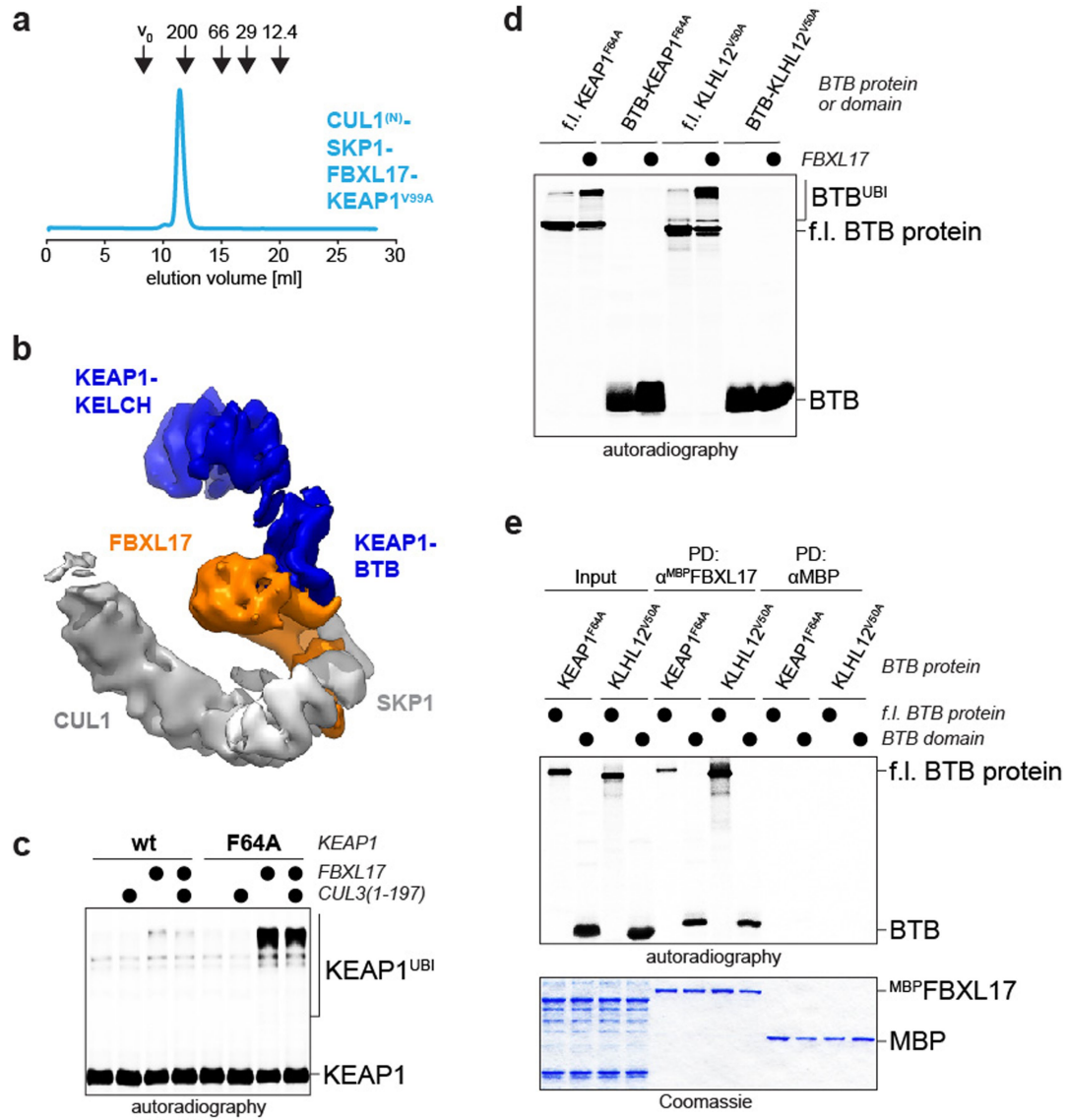
Three independent experiments were performed with similar results. **d**, BTB domains of wild-type KEAP1 and mutant KEAP1^{F64A} form homodimers in solution, as determined by SEC-MALS. This experiment was performed twice. **e**, Mutant BTB domains unfold via an intermediate species. Wild-type or mutant BTB domains of KEAP1 (0.04 mg/ml) were incubated with various concentrations of urea, equilibrated overnight, and their resulting secondary structure was monitored by ellipticity at 222 nm using circular dichroism. The experiment was performed once for the mutants and twice for the wild-type KEAP1. **f**, The intermediate seen in the unfolding of KEAP1^{V98A} probably reflects local conformational changes, rather than monomerization. Urea-dependent unfolding curves for the BTB domain of KEAP1^{V98A} were repeated at tenfold higher BTB concentration (low: 0.04 mg/ml; high: 0.4 mg/ml); only the second transition shifted to higher urea concentrations, identifying it as a dimer-unfolded transition. This experiment was performed once. **g**, Mutation of Phe64 or Val98 to Ala in the BTB domain of KEAP1 reduces contacts between helices of two interacting subunits of the KEAP1 dimer.



Extended Data Fig. 2 | Cryo-EM data collection and processing.

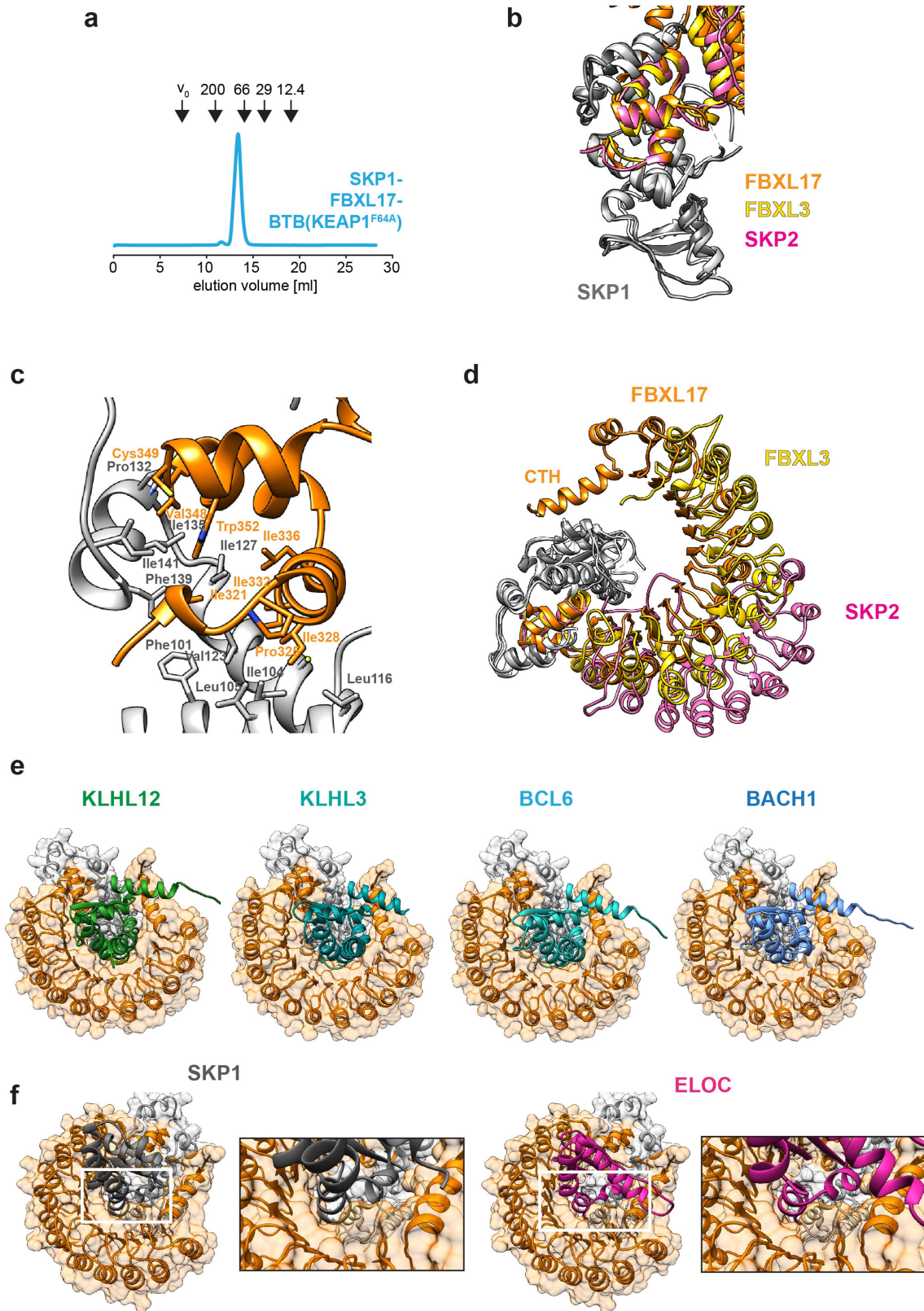
a, Representative micrograph (graphene oxide coated grid, imaged using a Talos Arctica and a Gatan K3 camera) showing CUL1-SKP1-FBXL17-KEAP1^{198A} particles. **b**, Resolution estimation using the FSC = 0.143 criterion⁵⁰ indicates an overall resolution of 8.5 Å for the cryo-EM reconstruction. **c**, Data processing scheme. Datasets were initially processed independently and then combined for the final refinement. EM volumes are shown in grey and

orientation distributions are given for intermediate refinement steps. The final reconstruction is shown with and without sharpening applied, and additionally colored by local resolution (determined using RELION3). **d**, **e**, Initial model generation. We originally obtained an initial reference by generating a low-resolution volume with the overall shape of the complex observed in 2D class averages (**d**) and later also verified this solution using CRYOSPARC2 ab initio model generation (**e**; see Methods for details).



Extended Data Fig. 3 | SCF^{FBXL17} binds the BTB domain, but its active site is next to the Kelch repeats of KEAP1 **a**, Elution profile of the SCF^{FBXL17}-KEAP1^{V98A} complex by size exclusion chromatography detecting A₂₈₀. Control proteins with known MW are shown on top. This experiment was performed three times. **b**, Cryo-EM density map of the SCF^{FBXL17}-KEAP1^{V98A} complex. Dark grey: CUL1¹⁻⁴⁵⁰; light grey: SKP1; orange: FBXL17; blue: KEAP1. **c**, Despite an overlap in binding sites, CUL3 does not compete with SCF^{FBXL17} for substrate ubiquitylation. ³⁵S-labelled wild-type or mutant KEAP1 were ubiquitylated by SCF^{FBXL17} in reticulocyte lysate either in the presence or absence of a CUL3 variant shown to bind BTB proteins. Ubiquitylated KEAP1 was detected by gel electrophoresis and autoradiography. Three independent experiments were performed with similar results. **d**, SCF^{FBXL17} ubiquitylates full-length BTB

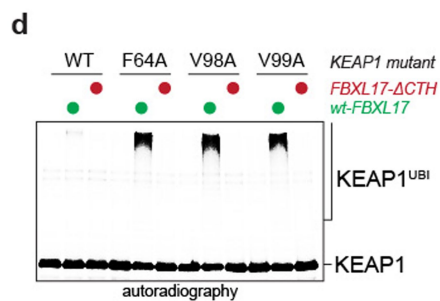
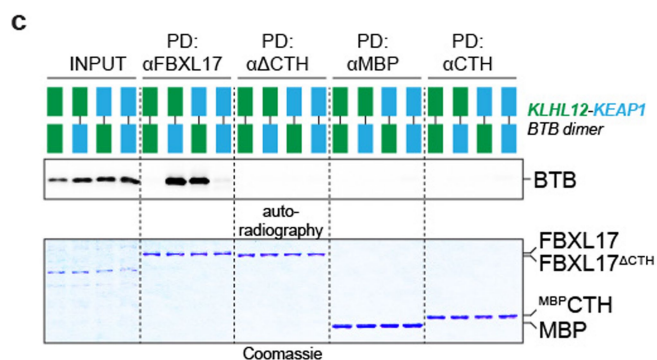
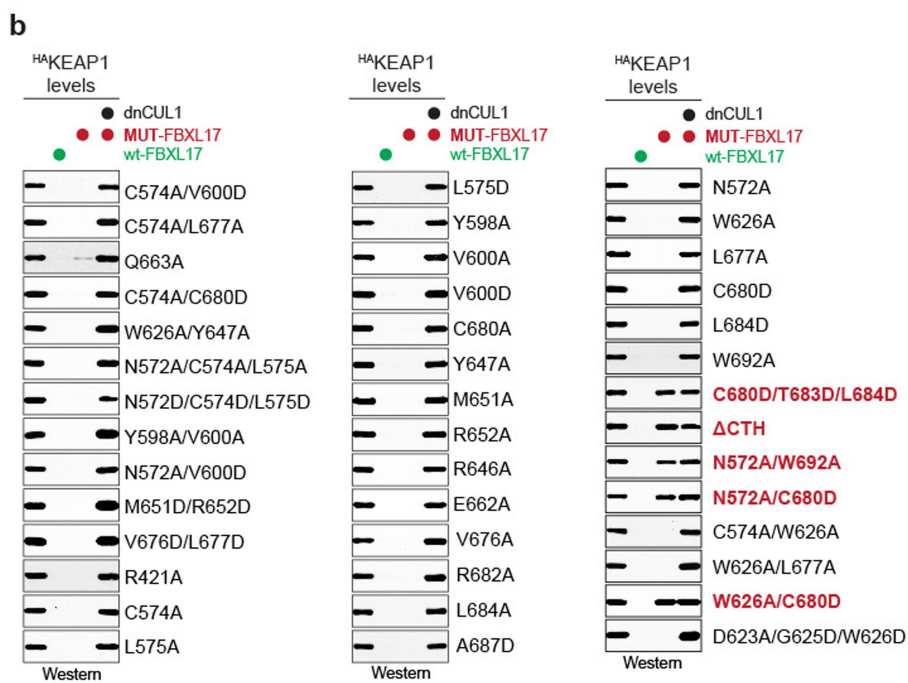
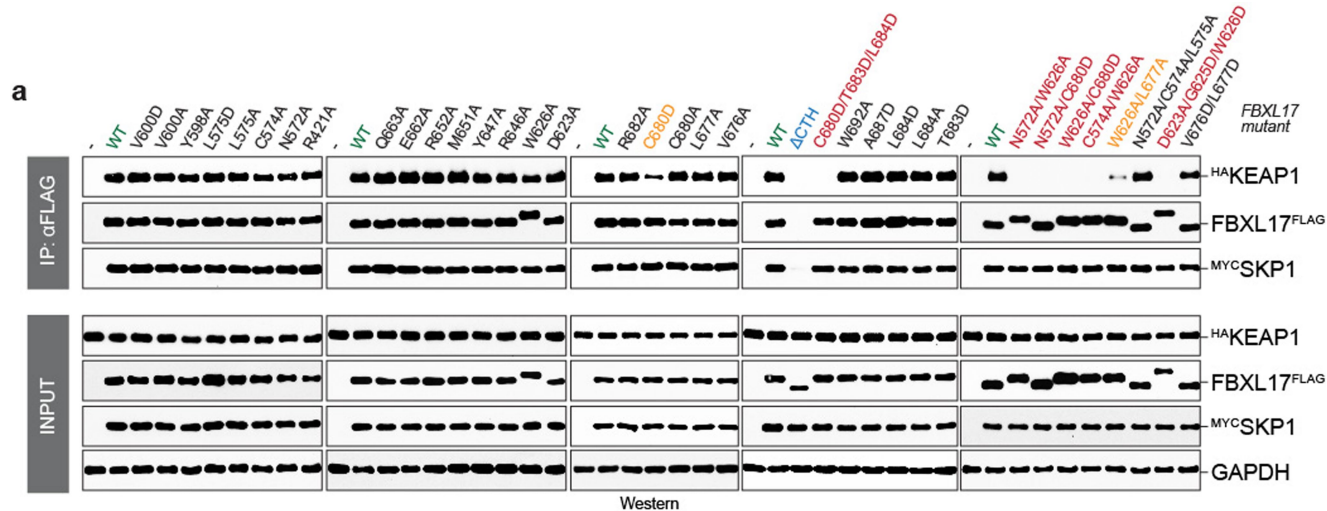
proteins with Kelch repeats better than isolated BTB domains. ³⁵S-labelled full-length KEAP1^{F64A}, the BTB domain of KEAP1^{F64A}, full-length KLHL12^{V50A}, or the BTB domain of KLHL12^{V50A} were incubated in reticulocyte lysate with recombinant FBXL17, and ubiquitylation was detected by gel electrophoresis and autoradiography. Two independent experiments were performed with similar results. **e**, Full-length BTB proteins or isolated BTB domains bind similarly well to FBXL17. ³⁵S-labelled full-length BTB proteins or isolated BTB domains, as indicated on the right, were incubated with immobilized MBPFBXL17 and bound proteins were detected by gel electrophoresis and autoradiography. Two independent experiments were performed with similar results.



Extended Data Fig. 4 | See next page for caption.

Extended Data Fig. 4 | Structural features of the SKP1/FBXL17-BTB complex. **a**, Elution profile of the SKP1/FBXL17-BTB(KEAP1^{F64A}) complex by size exclusion chromatography detecting A₂₈₀. Control proteins with known MW are shown on top. This experiment was performed three times. **b**, FBXL17 binds to SKP1 via its F-box domain, in a manner highly similar to the LRR-domain containing F-box proteins SKP2 and FBXL3^{20,21}. The structures of SKP1-FBXL17, SKP1-SKP2, and SKP1-FBXL3 were aligned via SKP1. FBXL17 is shown in orange, SKP2 in magenta, and FBXL3 in yellow. **c**, FBXL17 uses conserved residues in its F-box to bind SKP1. The highlighted residues in FBXL17 (orange)

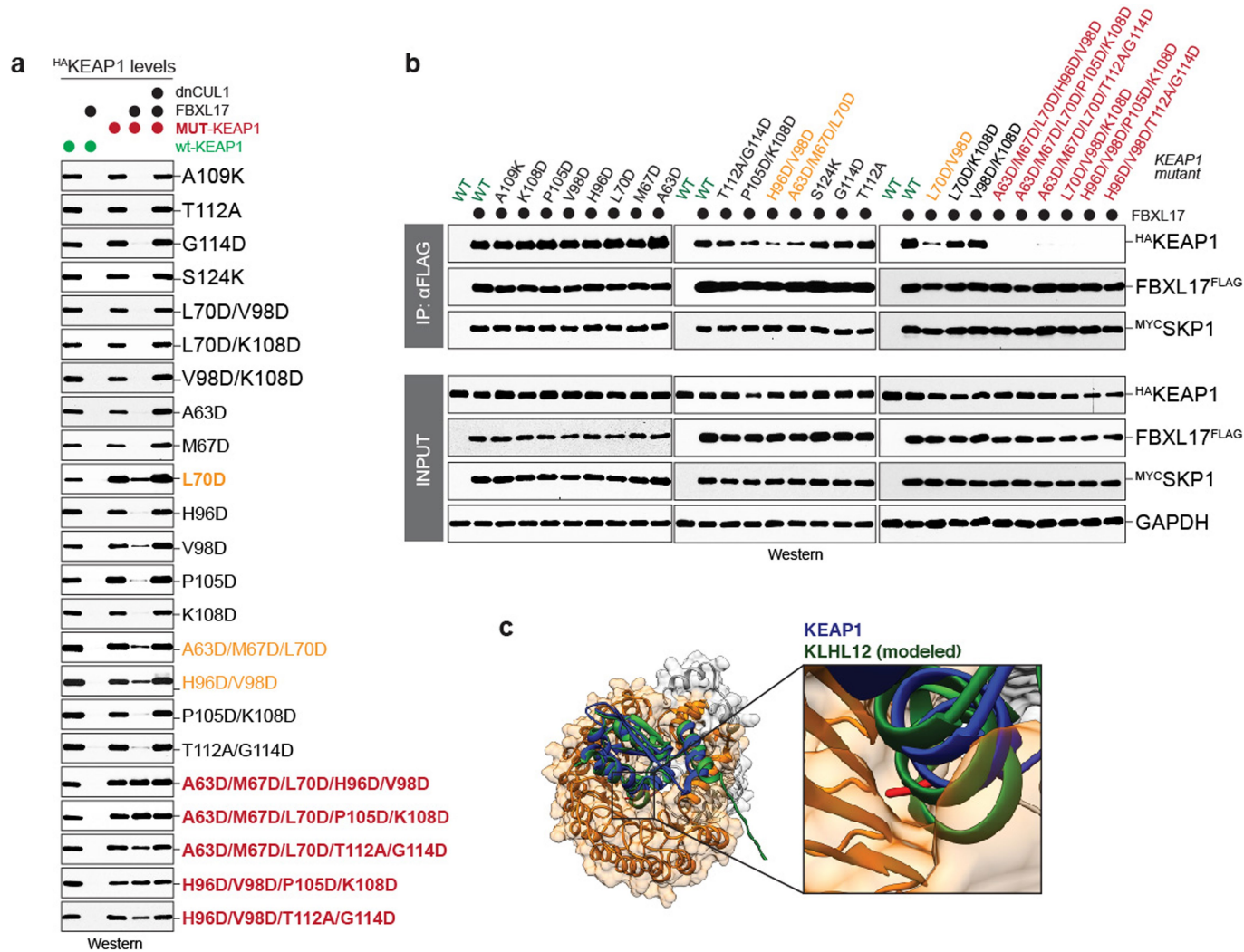
that bind SKP1 (grey) were adopted from ref. ²¹. **d**, The substrate binding LRR domain of FBXL17 is longer and more curved than the LRR domains of SKP2 or FBXL3. Complexes were aligned via SKP1 (FBXL17, orange; SKP2, magenta; FBXL3, yellow). **e**, Structural models of BTB-FBXL17 complexes, using BTB domains that are similar in shape, but distinct in sequence. All complexes between FBXL17 and these confirmed substrates² can be formed without steric clashes. **f**, SKP1 and Elongin C, which also adopt BTB folds, cannot be bound to FBXL17, due to steric clashes shown in the insets.



Extended Data Fig. 5 | See next page for caption.

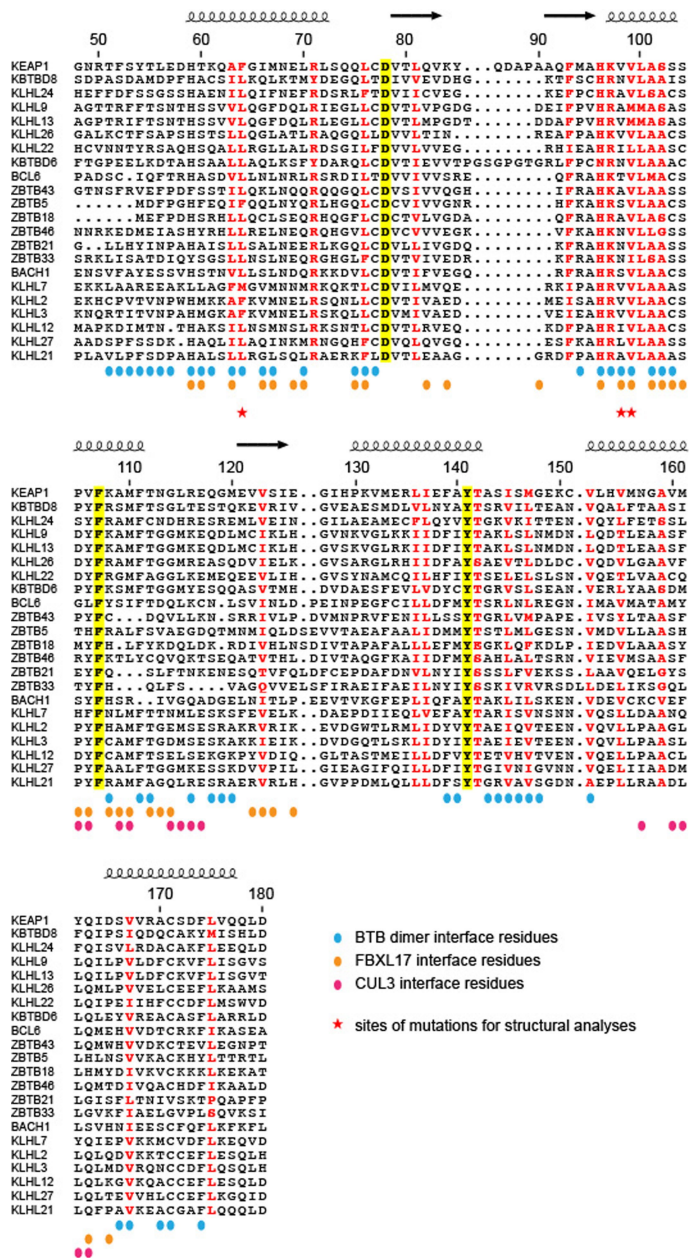
Extended Data Fig. 5 | Validation of SKP1/FBXL17-BTB structure through FBXL17 mutations. **a**, Single mutations of FBXL17 rarely affect co-translational recognition of KEAP1 in cells. FBXL17^{FLAG} mutants were affinity-purified from 293T cells that also expressed MYC-SKP1, HA-KEAP1, and dominant negative CUL1 to prevent degradation of the BTB protein. Bound proteins were detected by gel electrophoresis and western blotting. Red, mutations that abolish binding to FBXL17; orange, mutations that weaken binding to FBXL17; green, wild-type FBXL17; black: mutations that had no effect on KEAP1 binding. This experiment was performed once. **b**, Single mutations of FBXL17 rarely interfere with the proteasomal degradation of KEAP1. 293T cells were transfected with HA-KEAP1 and either wild-type or mutant FBXL17^{FLAG}, as denoted on the right, MYC-SKP1, and dominant-negative CUL1 (dnCUL1), as indicated. The abundance of KEAP1 was monitored by gel electrophoresis and α HA-Western blotting. This

experiment was performed once. **c**, The CTH is required, but not sufficient, for BTB recognition by SCF^{FBXL17}. Immobilized recombinant MBP, MBP-FBXL17, MBP-FBXL17^{CTH}, or CTH^{MBP} were incubated with ³⁵S-labelled fused dimers of the BTB domains of KLHL12 (green) and KEAP1 (orange). Bound proteins were detected by gel electrophoresis and autoradiography. This experiment was performed once. **d**, The CTH is required for in vitro ubiquitylation of mutant KEAP1. Recombinant FBXL17-SKP1 or FBXL17^{CTH}-SKP1 were added to reticulocyte lysate after the synthesis of either wild-type or mutant KEAP1. Reticulocyte lysate contains all other components required for in vitro ubiquitylation through SCF^{FBXL17}. Unmodified and ubiquitylated KEAP1 were detected by gel electrophoresis and autoradiography. This experiment was performed once.

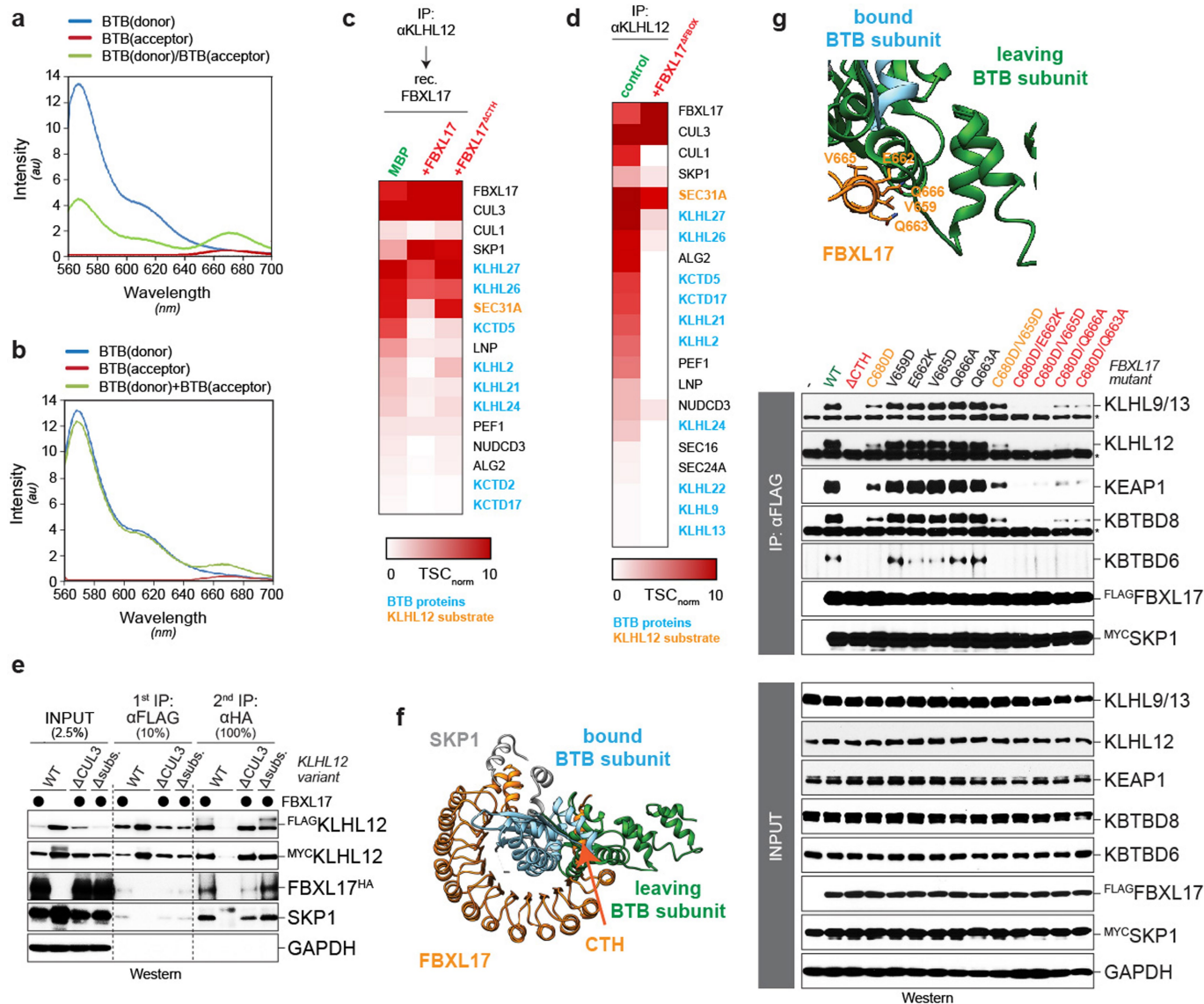


Extended Data Fig. 6 | Validation of SKP1/FBXL17-BTB structure through KEAP1 mutations. **a**, Single mutations in KEAP1 do not inhibit the co-translational SCF^{FBXL17}-dependent degradation of the BTB protein. 293T cells were transfected with either wild-type (left three lanes) or mutant ^{HA}KEAP1 (right two lanes; mutations denoted on the right), as well as ^{MYC}SKP1, FBXL17^{FLAG} and dominant negative CUL1 (dnCUL1), as indicated on top. KEAP1 levels were monitored by gel electrophoresis and α HA western blotting. This experiment was performed once. **b**, Single mutation of residues in KEAP1 at the interface

with FBXL17 do not inhibit co-translational binding of the BTB protein to SCF^{FBXL17}. 293T cells were transfected with wild-type or mutant ^{HA}KEAP1, ^{MYC}SKP1, FBXL17^{FLAG}, and dominant-negative CUL1 (dnCUL1). FBXL17^{FLAG} was affinity-purified and bound proteins were detected by gel electrophoresis and western blotting. This experiment was performed once. **c**, Ala109 (red stick) in KEAP1 (blue) is positioned further from FBXL17 compared to the corresponding A60 residue in KLHL12 (green). KEAP1 and KLHL12 BTB domains were overlain bound to FBXL17 (*KEAP1*, actual structure; *KLHL12*, model).

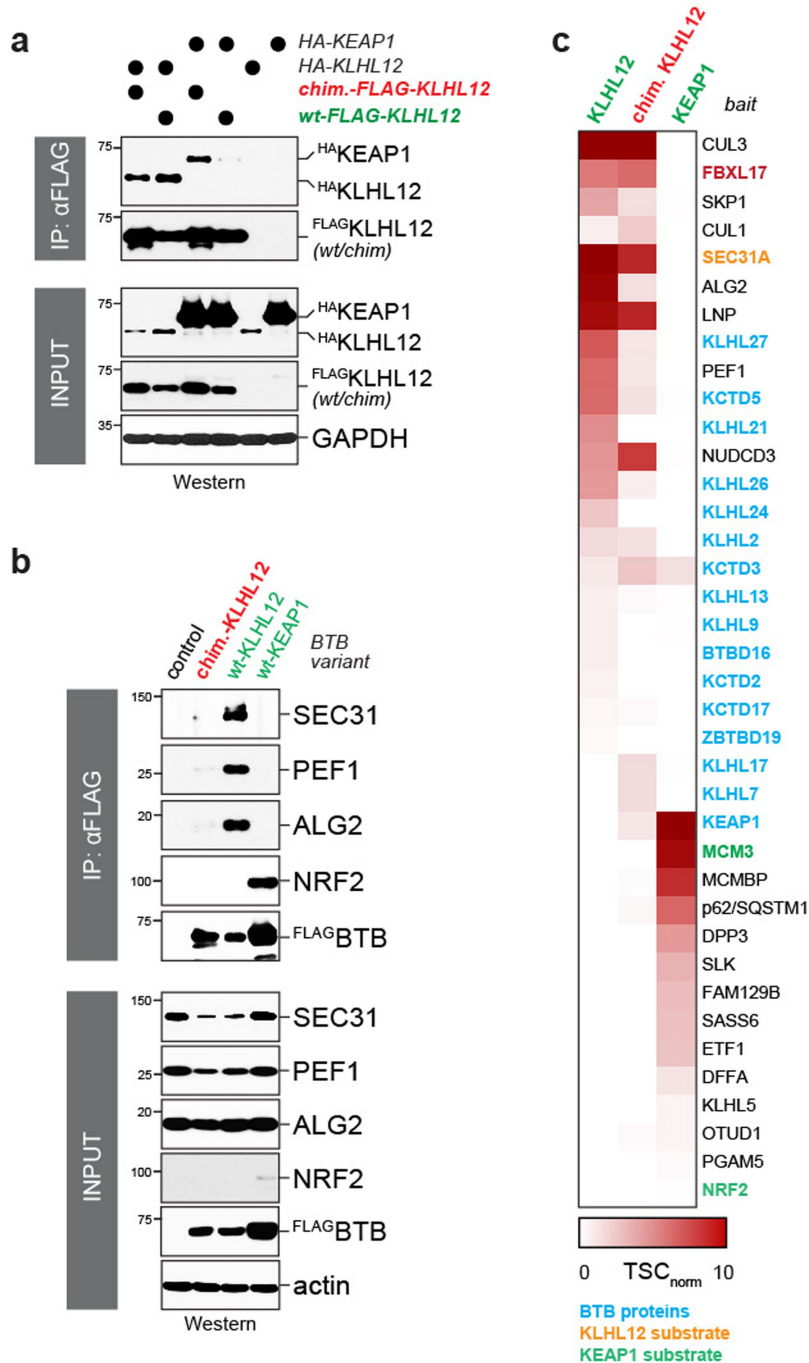


Extended Data Fig. 7 | Sequence alignment of BTB domains. Residues involved in BTB dimerization are marked by a blue dot; residues at the interface between the BTB domain and FBXL17 are marked by an orange dot; residues at the interface between the BTB domain and CUL3 are marked by a magenta dot. Sites of mutations used for X-ray crystallography or electron microscopy are marked by a red star.



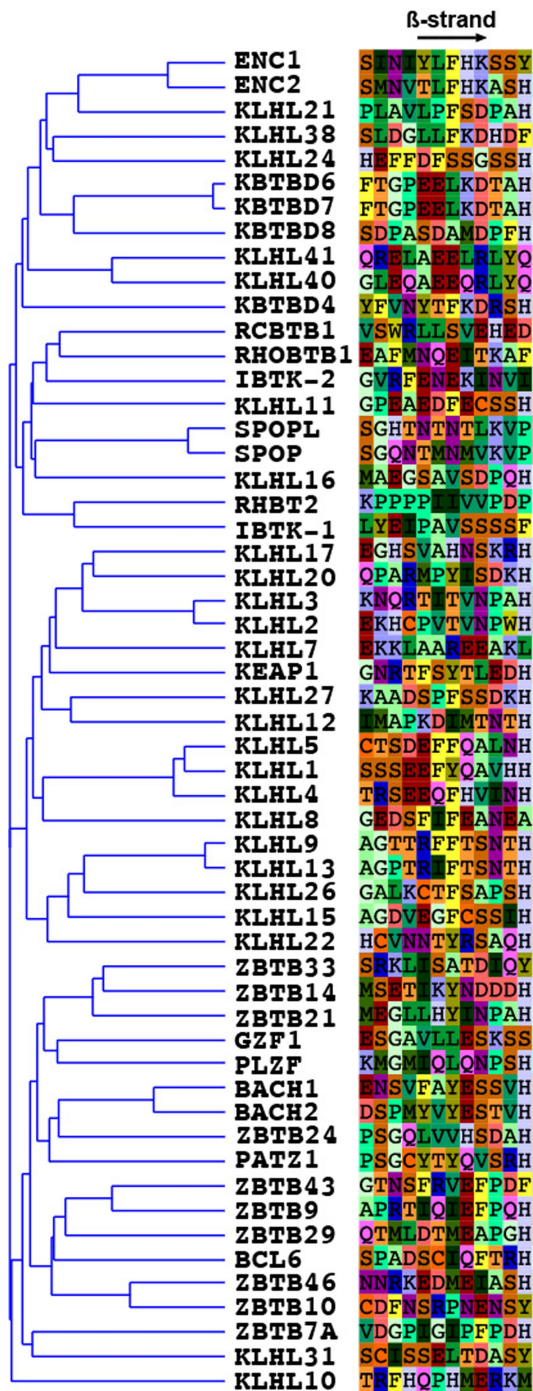
Extended Data Fig. 8 | Binding and destabilization of BTB dimers by SCF^{FBXL17}. **a**, FRET-based assay to monitor BTB dimer formation. Blue curve: The BTB domain of KEAP1^{F64A} was labelled with Alexa 555, then denatured and refolded. Red curve: The BTB domain of KEAP1^{F64A} was labelled with Alexa 647, then denatured and refolded. Green curve: Two separate BTB domain pools of KEAP1^{F64A} were labelled with either Alexa 555 or Alexa 647, mixed in equimolar concentrations, denatured, and then refolded. About 50% of dimers are labelled with distinct fluorophores in each BTB subunit, giving rise to donor fluorescence quenching and acceptor emission as indication of FRET. Three independent experiments were performed with similar results. **b**, KEAP1^{F64A} dimers dissociate very slowly and inefficiently. BTB domains of KEAP1^{F64A} were labelled with either Alexa 555 or Alexa 647, respectively. The labelled BTB domains were then mixed, incubated overnight, and analysed for FRET that results from stochastic rebinding of BTB monomers, leading to formation of BTB dimers containing one subunit labelled with Alexa 555 and the other subunit labelled with Alexa 647. However, in comparison to complex reformation by refolding (see above), little FRET was detected. This experiment was performed twice. **c**, FBXL17 can modulate BTB complex composition in vitro. The *KLHL12* locus was tagged with a 3xFLAG epitope by CRISPR/Cas9-mediated genome editing. Endogenous KLHL12^{3xFLAG} complexes were affinity-purified from 293T cells and incubated with recombinant MBP

(control), FBXL17, or inactive FBXL17^{ΔCTH}. Proteins that remained bound to KLHL12^{3xFLAG} were determined by mass spectrometry. **d**, Overexpression of FBXL17^{ΔFB}, which can bind but not ubiquitylate BTB proteins, prevents BTB heterodimerization. The endogenous KLHL12^{3xFLAG} was affinity-purified either in the presence or absence of FBXL17^{ΔFB}, and bound proteins were determined by mass spectrometry. **e**, FBXL17 can bind BTB dimers. FLAG-KLHL12 was affinity-purified from 293T cells also expressing MYC-KLHL12 and FBXL17^{HA}. FLAG-KLHL12 complexes were eluted with FLAG-peptide and FBXL17^{HA}-containing complexes were then purified over αHA-agarose. Bound MYC-KLHL12, indicative of FBXL17 associating with KLHL12 dimers, was then detected by western blotting. This experiment was performed once. **f**, Binding of FBXL17 to BTB dimers requires its CTH to be disengaged from its binding site at the BTB dimer interface. A structural model of a KEAP1 BTB dimer bound to FBXL17 was generated using the KEAP1^{F64A} dimer and the FBXL17-KEAP1^{F64A} complex structures. Clashes are predominantly at the CTH of FBXL17. **g**, Residues of FBXL17, which in the structural model of a FBXL17-BTB dimer complex are in proximity to the leaving BTB subunit, contribute to stable substrate recognition. Indicated FBXL17 residues at the interface with the leaving BTB subunit (above) were mutated in the sensitized background of the FBXL17^{C680D} variant and analysed for binding to endogenous BTB proteins by affinity purification and western blotting. This experiment was performed once.



Extended Data Fig. 9 | The N-terminal β -strand is important for BTB complex formation and recognition. **a**, Chimeric KLHL12 with β -strand and adjacent dimer interface residues of KEAP1, but not wild-type KLHL12, forms heterodimers with KEAP1 in vivo. 293T cells were transfected with KLHL12^{FLAG} (wild-type or chimaera) and KLHL12^{HA} or HA-KEAP1, as indicated. KLHL12^{FLAG} variants were immunoprecipitated and bound proteins detected by gel electrophoresis and western blotting. This experiment was performed once. **b**, BTB heterodimers are inactive in signalling. 293T cells were transfected with FLAG-tagged wild-type KLHL12, chimeric KLHL12, or wild-type KEAP1. The

FLAG-tagged BTB proteins were affinity-purified and bound endogenous targets of KLHL12 (SEC31, PEF1, ALG2) or KEAP1 (NRF2) were detected by western blotting. This experiment was performed once. **c**, A chimeric KLHL12 that contains helix and β -strand residues of KEAP1 efficiently heterodimerizes with KEAP1, yet fails to bind substrates of either KLHL12 or KEAP1. KLHL12^{FLAG}, chimeric KLHL12^{FLAG} or KEAP1^{FLAG} were affinity-purified from 293T cells and bound proteins were determined by CompPASS mass spectrometry. This experiment was performed in two technical replicates with similar results.



Extended Data Fig. 10 | The amino-terminal β -strand of BTB domains serves as a molecular barcode for functional dimerization. Sequence alignment of amino-terminal β -strands across human BTB domains shows divergence, indicative of rapid evolution of this protein sequence.

Extended Data Table 1 | Data collection and refinement statistics for crystal structures.

	KEAP1 ^{BTB}	KEAP1 ^{BTB} F64A	KEAP1 ^{BTB} V98A	KEAP1 ^{BTB} F64A - FBXL17 - SKP1
Data collection				
Beamline	ALS 8.3.1	ALS 8.3.1	ALS 8.3.1	ALS 8.3.1
Space Group	<i>P6₅22</i>	<i>P6₅22</i>	<i>P6₅22</i>	<i>P3₂21</i>
Cell dimensions				
a, b, c (Å)	42.68, 42.68, 266.24	42.64, 42.64, 264.85	42.62, 42.62, 268.46	183.6, 183.6, 55.4
α, β, γ (°)	90, 90, 120	90, 90, 120	90, 90, 120	90, 90, 120
Resolution (Å)	44.37-2.20 (2.27-2.20)	44.14-2.50 (2.60-2.50)	36.91-2.55 (2.66-2.55)	159.06-3.207 (3.43-3.21)
No. unique reflections	8147 (772)	5502 (448)	5358 (522)	17739 (1711)
<i>R</i> _{merge}	0.198 (3.835)	0.172 (1.878)	0.167 (3.271)	0.289 (4.145)
<i>I</i> / <i>σ</i> <i>I</i>	16.1 (1.1)	11.3 (1.0)	11.9 (0.8)	7.6 (0.7)
<i>CC</i> _{1/2}	1 (0.713)	1 (0.617)	1 (0.405)	1 (0.452)
Completeness (%)	99.78 (99.61)	97.95 (86.99)	99.39 (98.10)	98.44 (89.46)
Redundancy	24.5 (26.4)	11.8 (8.2)	9.6 (9.5)	10.6 (10.2)
Refinement				
Resolution (Å)	44.37-2.20 (2.28-2.20)	44.14-2.50 (2.59-2.50)	36.91-2.55 (2.64-2.55)	79.529-3.207 (3.32-3.21)
No. reflections	8129 (769)	5493 (447)	5349 (516)	17524 (1579)
<i>R</i> _{work}	0.2382 (0.3330)	0.2331 (0.2878)	0.2543 (0.4043)	0.2456 (0.4179)
<i>R</i> _{free}	0.3053 (0.4307)	0.2929 (0.3545)	0.3114 (0.4334)	0.2891 (0.4232)
No. atoms	1029	1017	1015	5219
Protein	1006	1000	1012	5219
Ligand/ion	0	0	0	0
Water	23	17	3	0
Wilson <i>B</i> factor (Å ²)	46.52	51.83	66.68	101.91
Average <i>B</i> factor (Å ²)	55.82	55.33	69.61	122.25
Protein	55.96	55.47	69.66	122.25
Water	49.81	47.33	51.36	-
R.M.S deviations				
Bond lengths (Å)	0.0069	0.0015	0.0039	0.0018
Bond angles (°)	0.85	0.44	1.01	0.43
Ramachandran plot				
Favored [%]	97.64	100	96.06	90.78
Allowed [%]	2.36	0	2.36	8.76
Outliers [%]	0	0	1.80	0.46

Table shows crystallography refinement data. Values in parentheses are for the highest-resolution shell.

Reporting Summary

Nature Research wishes to improve the reproducibility of the work that we publish. This form provides structure for consistency and transparency in reporting. For further information on Nature Research policies, see [Authors & Referees](#) and the [Editorial Policy Checklist](#).

Statistics

For all statistical analyses, confirm that the following items are present in the figure legend, table legend, main text, or Methods section.

n/a Confirmed

- | | | |
|-------------------------------------|-------------------------------------|--|
| <input type="checkbox"/> | <input checked="" type="checkbox"/> | The exact sample size (n) for each experimental group/condition, given as a discrete number and unit of measurement |
| <input type="checkbox"/> | <input checked="" type="checkbox"/> | A statement on whether measurements were taken from distinct samples or whether the same sample was measured repeatedly |
| <input checked="" type="checkbox"/> | <input type="checkbox"/> | The statistical test(s) used AND whether they are one- or two-sided
<i>Only common tests should be described solely by name; describe more complex techniques in the Methods section.</i> |
| <input checked="" type="checkbox"/> | <input type="checkbox"/> | A description of all covariates tested |
| <input checked="" type="checkbox"/> | <input type="checkbox"/> | A description of any assumptions or corrections, such as tests of normality and adjustment for multiple comparisons |
| <input checked="" type="checkbox"/> | <input type="checkbox"/> | A full description of the statistical parameters including central tendency (e.g. means) or other basic estimates (e.g. regression coefficient) AND variation (e.g. standard deviation) or associated estimates of uncertainty (e.g. confidence intervals) |
| <input checked="" type="checkbox"/> | <input type="checkbox"/> | For null hypothesis testing, the test statistic (e.g. F , t , r) with confidence intervals, effect sizes, degrees of freedom and P value noted
<i>Give P values as exact values whenever suitable.</i> |
| <input checked="" type="checkbox"/> | <input type="checkbox"/> | For Bayesian analysis, information on the choice of priors and Markov chain Monte Carlo settings |
| <input checked="" type="checkbox"/> | <input type="checkbox"/> | For hierarchical and complex designs, identification of the appropriate level for tests and full reporting of outcomes |
| <input checked="" type="checkbox"/> | <input type="checkbox"/> | Estimates of effect sizes (e.g. Cohen's d , Pearson's r), indicating how they were calculated |

Our web collection on [statistics for biologists](#) contains articles on many of the points above.

Software and code

Policy information about [availability of computer code](#)

Data collection

Electron microscopy:

Electron micrograph movies were drift-corrected and dose-weighted using MOTIONCOR2 from within FOCUS (v1.1.0), or the motion correction algorithm implemented in RELION3. CTF parameters were estimated using GCTF (carbon support dataset) and CTFFIND4 (graphene oxide dataset) from within RELION3, identifying 380 and 538 micrographs from the graphene oxide and carbon support datasets showing suitable quality than rings, respectively.

X-ray Crystallography:

Data were processed using XDS (version Jan 26, 2018) and scaled and merged with Aimless (v0.7.1) in CCP4 (v7.0.058). Structures were solved by molecular replacement using Phenix Phaser (v2.8.2).

Quantitative Western Blotting:

Data were acquired using Image Studio (v 5.2.5).

Data analysis

Electron microscopy:

To interpret the cryo-EM map, we docked the atomic structures of the SKP1-FBXL17-KEAPBTB complex (this work) as well as the structures of human SKP1 and CUL1 (PDB ID 1LDK) as rigid bodies using UCSF CHIMERA (v1.13). We ran one macro cycle of PHENIX (v1.16) real space refinement in order to resolve clashes at the interface of the docked models.

X-ray crystallography:

Manual model building was performed in COOT (v0.8.9.1) and models were refined using Phenix refine (v1.14). The initial SKP1/FBXL17/KEAP1-BTB complex model was improved using Phenix Rosetta Refine. The software used was curated by SBGrid.

Structural analysis:

The PISA server (<https://www.ebi.ac.uk/pdbe/pisa/>) was used to calculate surface interactions between the KEAP1 subunit and FBXL17, the opposing KEAP1 subunit, or CUL3 in their corresponding structures. The model of a KEAP1-KLHL12 heterodimer was determined by first obtaining a KLHL12 homodimer model from the SWISS-model server (<https://swissmodel.expasy.org>). The map of conservation within the BTB domain was determined by producing a sequence alignment using ClustalX (v2.1) of 22 BTB substrates of FBXL17. Then the surface of KEAP1 was colored by mavConservation according to a red-white-blue color scheme in CHIMERA (v1.11). Structural alignments of the KEAP1 BTB domains and the Skp1/F-box structures were performed in Chimera (v1.11).

The sequence alignment of the N-terminal beta strand was created using ClustalX (v2.1) with manual adjustment in Jalview (v2.10.5). A neighbor-joining tree (of the full BTB domain) was calculated in Jalview using a BLOSUM62 scoring matrix. The N-J tree was then displayed using T-rex (<http://www.trex.uqam.ca>) and the sequence alignment of the beta-strand region (KEAP1 residues 48-59) was colored by residue in Jalview. A smaller number of BTB sequences was used in the full BTB alignment and were displayed using ESPrnt 3 (<http://esprnt.ibcp.fr/ESPrnt/ESPrnt/>).

Mass spectrometry:

To generate the interaction heatmap, the normalized total spectral counts of select interactors in FBXL17 or BTB IPs were plotted and higher values were set to 10 using default parameters of Morpheus, <https://software.broadinstitute.org/morpheus>.

Binding analysis:

Band intensities were quantified in ImageJ (v1.51r), values were plotted in GraphPad Prism (v8.3.0), and binding affinity was calculated using a non-linear fit and binding-saturation equation.

Circular dichroism and FRET:

CD and FRET graphs were generated using R (version 3.3.3).

For manuscripts utilizing custom algorithms or software that are central to the research but not yet described in published literature, software must be made available to editors/reviewers. We strongly encourage code deposition in a community repository (e.g. GitHub). See the Nature Research [guidelines for submitting code & software](#) for further information.

Data

Policy information about [availability of data](#)

All manuscripts must include a [data availability statement](#). This statement should provide the following information, where applicable:

- Accession codes, unique identifiers, or web links for publicly available datasets
- A list of figures that have associated raw data
- A description of any restrictions on data availability

The atomic coordinates of the CUL1-SKP1-FBXL17-KEAP1(V99A) complex has been deposited to Protein Data Bank with accession number 6WCQ. The respective cryo-EM map has been deposited to the Electron Microscopy Data Bank with accession number EMD-21617. The atomic coordinates of the X-ray crystal structures have been deposited to the Protein Data Bank with the following accession numbers: 6W66 (KEAP1-S172A/F64A -FBXL17-SKP1 complex), 6W67 (KEAP1-S172A), 6W68 (KEAP1-S172A/V98A), and 6W69 (KEAP1-S172A/F64A). Uncropped gel images are shown in Supplementary Figures 1 and 2.

Field-specific reporting

Please select the one below that is the best fit for your research. If you are not sure, read the appropriate sections before making your selection.

Life sciences Behavioural & social sciences Ecological, evolutionary & environmental sciences

For a reference copy of the document with all sections, see [nature.com/documents/nr-reporting-summary-flat.pdf](https://www.nature.com/documents/nr-reporting-summary-flat.pdf)

Life sciences study design

All studies must disclose on these points even when the disclosure is negative.

Sample size	No methods were used to predetermine sample size for experiments. For cellular assays all samples were normalized to the same total protein concentration.
Data exclusions	No data were excluded from biochemical experiments. For crystallography experiments, we solved the structure using the highest-quality diffraction dataset that we collected. Cryo-EM particles were picked based on the Laplacian-of-Gaussian algorithm implemented in RELION3
Replication	Cell culture and biochemistry experiments were usually performed twice and were often validated by complementary experiments (e.g. interaction and degradation experiments in Figure 3). The X-ray crystal structure of the complex was independently determined from the cryo-EM structure and the results validated one another.
Randomization	Since most of the experiments were structural, this is not applicable.
Blinding	We did not have animal-based experiments and therefore our experiments are not applicable for blinding.

Reporting for specific materials, systems and methods

We require information from authors about some types of materials, experimental systems and methods used in many studies. Here, indicate whether each material, system or method listed is relevant to your study. If you are not sure if a list item applies to your research, read the appropriate section before selecting a response.

Materials & experimental systems

n/a	Involvement	Material
<input type="checkbox"/>	<input checked="" type="checkbox"/>	Antibodies
<input type="checkbox"/>	<input checked="" type="checkbox"/>	Eukaryotic cell lines
<input checked="" type="checkbox"/>	<input type="checkbox"/>	Palaeontology
<input checked="" type="checkbox"/>	<input type="checkbox"/>	Animals and other organisms
<input checked="" type="checkbox"/>	<input type="checkbox"/>	Human research participants
<input checked="" type="checkbox"/>	<input type="checkbox"/>	Clinical data

Methods

n/a	Involvement	Method
<input checked="" type="checkbox"/>	<input type="checkbox"/>	ChIP-seq
<input checked="" type="checkbox"/>	<input type="checkbox"/>	Flow cytometry
<input checked="" type="checkbox"/>	<input type="checkbox"/>	MRI-based neuroimaging

Antibodies

Antibodies used

anti-FLAG (CST, #2368, 1:5000, Lot 12), anti-HA (CST, #3724, clone C29F4, 1:15000, Lot 9), anti-c-Myc (Santa Cruz, #sc-40, clone 9E10), anti-GAPDH (CST, #2118, clone 14C10, 1:15000), anti-beta-Actin (MP Biomedicals, #691001, clone C4, 1:20000, Lot 04917), anti-SEC31A (BD, #612350, Clone 32/Sec31A, 1:500), anti-PEF1 (Abcam, #ab137127, clone EPR9310, 1:500), ALG2/PDCD6 (Proteintech, #12303-1-AP, Clone AG2949, 1:500), anti-NRF2 (CST, #12721, clone D129C, 1:1000), anti-KLHL12 (CST, #9406, clone 2G2, 1:1000), anti-KEAP1 (CST, #7705, Clone D1G10, 1:1000), anti-KLHL9/13 (Santa Cruz, #166486, Clone D-4, 1:1000), anti-KBTBD6 (Abnova, #690867, Clone H00089890-B01P, 1:500). The anti-KBTBD8 antibody was generated previously (1:250) (Werner et al., 2015). For fluorescent Western blot analysis secondary antibodies IRDye 800CW anti-rabbit (Li-Cor, #926-32211, 1:20000, Lot C50033105) and IRDye 680RD anti-mouse (Li-Cor, #925-68070, 1:20000, Lot C90710-07).

Validation

Antibodies validated by recombinant proteins: anti-FLAG (#2368), anti-HA (#3724), anti-c-MYC (#40). Antibodies validated by the lab previously: anti-GAPDH (#2118), anti-beta-actin (#691001), anti-SEC31A (#612350), anti-PEF1 (#ab137127), anti-ALG2/PDCD6 (#12303-1-AP), anti-NRF2 (#12721), anti-KLHL12 (#9406), anti-KEAP1 (#7705), anti-KLHL9/13 (#166486), anti-KBTBD6 (#690867), anti-KBTBD8 (Werner et al., 2015).
Antibodies validated from manufacturer's site: IRDye 800CW anti-rabbit (#926-32211) was tested by ELISA and flow cytometry to react with the heavy and light chains of rabbit IgG, and with the light chains of rabbit IgM and IgA. IRDye 680RD anti-mouse (#925-68070) was tested by ELISA and flow cytometry to react with the heavy and light chains of mouse IgG1, IgG2a, IgG2b, and IgG3, and with the light chains of mouse IgM and IgA.

Eukaryotic cell lines

Policy information about [cell lines](#)

Cell line source(s)

HEK293T cells (UC Berkeley Cell Culture Facility)

Authentication

HEK293T cells were purchased directly from the UC Berkeley Cell Culture Facility (authenticated by short tandem repeat analysis)

Mycoplasma contamination

Cells tested negative for mycoplasma.

Commonly misidentified lines (See [ICLAC](#) register)

No commonly misidentified cell lines were used.